UNIVERSITY OF CALIFORNIA

Los Angeles

Cadmium Telluride and Grain Boundaries: a Preliminary Study

A thesis submitted in partial satisfaction of the

requirements for the degree Master of Science

in Chemistry

by

Michael Evan Liao

2017

ABSTRACT OF THE THESIS

Cadmium Telluride and Grain Boundaries: a Preliminary Study

by

Michael Evan Liao

Master of Science in Chemistry

University of California, Los Angeles, 2017

Professor Xiangfeng Duan, Chair

The efficacy of the $CdCl_2$ treatment on polycrystalline CdTe-based solar cells was discovered over a quarter of a century ago; and yet, the exact mechanism of this treatment is still not fully understood to this day. In fact, the lack of understanding stems from a debate on the exact role of grain boundaries in $CdCl_2$-treated CdTe solar cells. Some hypothesize that the $CdCl_2$-treatment causes grain boundaries to become beneficial to solar cell performance while others disagree and claim that the treatment simply mitigates the harmful effects of grain boundaries via passivation. A future goal of this project is to determine which, if either, hypothesis is correct by direct wafer bonding single crystalline CdTe. Direct wafer bonding of single crystalline materials would create only one grain boundary at the bonded interface. This approach allows the orientation and surface chemistry of interfaces to be controlled in order to study the chemistry of grain boundaries methodically. However, before any direct wafer bonding can be done, a preliminary study of single crystalline CdTe is necessary. High-quality direct

wafer bonding can only be achieved if the surfaces of each wafer satisfy certain requirements. Additionally, analyzing single crystalline CdTe materials prior to bonding is crucial in order to make any insightful connections between results found from direct bonding of single crystalline CdTe and what is observed in polycrystalline CdTe.

First, the surface of an (001) CdTe layer epitaxially grown on an (001) InSb substrate is studied using atomic force microscopy. Stacking faults on the CdTe surface are observed and the thickness of the grown CdTe epilayer is calculated by considering the interplanar angles between the (001) and (111) crystallographic planes as well as the dimensions of the stacking faults. While the stacking faults will inhibit successful wafer bonding, the roughness of the regions outside the stacking faults is 0.9 nm, which is an acceptable roughness for direct wafer bonding.

High resolution x-ray diffraction is used to study the strain of the CdTe epilayer at the epilayer-substrate interface by generating reciprocal space maps of the (004), (115), and (335) crystallographic planes. It is found that CdTe grown on an (001) InSb substrate at a low growth temperature exhibits nearly 0% relaxation. As a result, the in-plane lattice parameter of the CdTe layer is maximally strained to match the smaller lattice parameter of the InSb substrate. Consequently, the CdTe lattice is tetragonally strained normal to the substrate surface, which causes the out-of-plane lattice parameter of CdTe to be larger than its intrinsic value.

Lastly, a $CdCl_2$-treated CdTe-CdS (p-type CdTe on n-type CdS) solar cell structure is simulated using a semiconductor-heterojunction simulation program. In literature, it has been reported that chlorine atoms from the treatment segregate along grain boundaries in polycrystalline CdTe and cause the formation of local p-n junctions by inverting the grain boundaries to n-type. The simulated structure includes one grain and 2 grain boundaries. The grain/bulk CdTe material is p-type while the grain boundaries are made to be n-type with varying

doping concentrations. Both the conduction band and valence band energy exhibit downward sloping from the CdTe surface to the CdTe-CdS interface. This structure assumes that the grain boundaries are parallel to the CdTe-CdS interface. While these simulations do not prove the existence of the local type-inversion hypothesis, they do entertain a novel possibility for future devices fabrication methods.

The thesis of Michael Evan Liao is approved.

Mark S. Goorsky

Alexander M. Spokoyny

Xiangfeng Duan, Committee Chair

University of California, Los Angeles

2017

Table of Contents

Abstract of the Thesis ii
List of Figures vii
List of Tables x
Acknowledgements xi
Chapter 1: Introduction 1
1.1 Motivation 1
Chapter 2: Background and Theory 6
2.1 Atomic Force Microscopy 6
2.2 X-ray Diffraction and Reciprocal Space 8
2.3 Semiconductors and p-n Junctions 18
Chapter 3: Experiment 23
3.1 AFM: Surface Roughness and Stacking Fault Analysis 23
3.2 High-resolution X-ray Diffraction and Reciprocal Space Maps 23
3.3 Heterojunction Simulation 26
Chapter 4: Results and Discussion 29
4.1 AFM Results 29
4.2 HRXRD Results 32
4.3 Afors-Het Simulation Results 41
Chapter 5: Conclusion and Future Work 47
References 48

List of Figures

Figure 1. The energy profile of a grain boundary (vertical dotted line) for an n-type semiconductor. The interfacial energy states that capture majority carriers (electrons in this case) created by the grain boundary are represented by the gray box near the conduction band minimum (CBM). VBM stands for valence band maximum. Figure was inspired by Spencer et al. [5] 2

Figure 2. The energy profile of a grain boundary (vertical dotted line) in p-type CdTe. The median barrier (red) corresponds to a grain boundary before treatment. The smallest barrier (green) would occur if the $CdCl_2$ treatment passivates grain boundaries. The largest barrier (blue) would occur if the treatment inverts the grain boundary doping. Note that the Fermi level at the grain boundary is closer to the conduction band (n-type) while the Fermi level is closer to the valance band in the grain away from the boundary (p-type) 4

Figure 3. Schematic diagram of the AFM setup 7

Figure 4. A schematic diagram of planes of atoms exposed to a beam of monochromatic x-rays 9

Figure 5. Schematic diagram of XRD. ω is the angle between the incident x-ray beam and the sample surface (thin gray block on sample stage). 2θ is the angle of the detector. This diagram depicts a symmetric scan 10

Figure 6. Schematic diagram of the glancing incidence asymmetric scan. The dashed lines represent the crystallographic planes nonparallel to the sample surface that are inaccessible by symmetric scans 12

Figure 7. Schematic diagram of the glancing exit asymmetric scan. The dashed lines represent the crystallographic planes nonparallel to the sample surface that are inaccessible by symmetric scans 12

Figure 8. A scaled reciprocal space map sketch for CdTe. Inaccessible planes are those in the shaded gray regions. The x-ray wavelength used is Cu $K\alpha_1$, which is 1.54056 Å [16]. Note that planes accessible to G.E. scans are planes along the positive (right) side of the [110] zone axis and planes accessible to G.I. are found on the negative (left) side of this axis. Symmetric scans follow the vertical dashed line along the [001] direction 14

Figure 9. Angles ϕ and χ correspond to in-plane rotation and out-of-plane rotation, respectively. ω is shown as a point of reference from Figure 5 15

Figure 10. 100% relaxation (left) is the case where the epilayer is not strained at all by the substrate and is therefore not distorted. 0% relaxation (right) corresponds to a tetragonally distorted epilayer where the in-plane lattice parameter shrinks while the out-of-plane lattice parameter expands 17

Figure 11. Schematic band diagram of intrinsic and extrinsic semiconductors. The shaded purple (top) region is the conduction band and the shaded red (bottom) region is the valance band 19

Figure 12. The band diagram of the semiconductor from Figure 11 placed under bias. The positive end of the bias is on the left side of the band diagram 20

Figure 13. A p-type and an n-type semiconductor prior to forming a p-n junction 21

Figure 14. Band diagram of a p-n junction. Vertical dotted lines indicate the depletion region width 22

Figure 15. Schematic diagram of the high-resolution x-ray diffractometer used. Axis 1 is a beam conditioner that consists of a 3-bounce channel cut (111) silicon monochromator. Axis 2 is the sample stage (ω). Axis 3 is the detector and analyzer crystal; the analyzer crystal is a 4-bounce (220) channel cut silicon used to enhance resolution for TAD. For DAD, the crystal is moved out of the way of the x-ray beam 24

Figure 16: Reciprocal space maps are generated for the (004), (115), and (335) peaks 25

Figure 17. Structure used in Afors-Het. The grain boundaries are represented by red lines and are doped n-type. The bulk and grain of CdTe are both p-type and the CdS layer is n-type 27

Figure 18. The CdTe on InSb sample used in this study. The CdTe epilayer is the black region and the silver border at the CdTe's periphery is the exposed InSb substrate beneath the epilayer. The red square indicates the region of one of the five scans measured corresponding to Figure 19. The sample is 2.5 cm on edge 29

Figure 19. 40 μm by 40 μm AFM scan within the region indicated in Figure 18. The squares and lines (examples are circled in white) are stacking faults. The average RMS smoothness of regions outside the stacking faults is 0.9 nm 30

Figure 20. Schematic side profile of the square stacking faults on the CdTe epilayer. Note that crystallographic directions (vectors) are indicated in square brackets. These directions are orthogonal to their respective crystallographic planes, e.g. [001] direction is normal to the (001) plane [43] 31

Figure 21. Reciprocal space map of the (115) peaks. This map is on the same length scales as the other reciprocal space maps in Figure 22 and Figure 23 33

Figure 22. Reciprocal space map of the (004) peaks. This map is on the same length scales as the other reciprocal space maps in Figure 21 and Figure 23 34

Figure 23. Reciprocal space map of the (335) peaks. This map is on the same length scales as the other reciprocal space maps in Figure 21 and Figure 22 35

Figure 24. Simulation of (004) symmetric scans for various relaxation values for a 1.8 μm thick CdTe layer on an (001) InSb substrate. RADS is used to generate these curves. Maximum strain corresponds to 0% relaxation and zero strain corresponds to 100% relaxation 38

Figure 25. (004) peak separation as a function of relaxation determined by RADS simulations of a 1.8 μm CdTe layer on an (001) InSb substrate. 0% relaxation corresponds to a peak separation of 108.0" and 100% relaxation corresponds to a peak separation of 45.6" 39

Figure 26. ω:2θ symmetric scan of the (004) peaks. The lattice parameter of CdTe is larger than the lattice parameter of InSb, so the peak on the left is the (004) CdTe peak while the peak on the right is the (004) InSb peak. The peak separation is 108". Scan was done in TAD 40

Figure 27. The band diagram of a CdTe-CdS solar. E_C is the conduction band minimum, E_F is the Fermi level, and E_V is the valance band maximum. The total thickness of the CdTe layer is 5 μm, but the first two microns have been truncated in this plot to accentuate the much thinner 0.1 μm CdS layer 41

Figure 28. The band diagrams of doping grain boundaries n-type in a p-type bulk CdTe layer generated with Afors-Het. The grain size surrounded by the grain boundaries is 2 μm 42

Figure 29. Conduction band profile as a function of grain boundary doping. Since the conduction band and valence band are symmetrical, only the conduction band is shown for clarity. The doping ranges from 0 cm^{-3} to 10^{19} cm^{-3} starting from purple and ending in red, following a rainbow gradient 44

Figure 30. Average potential energy and average force as a function of grain boundary doping 45

Figure 31. Energy band diagram comparison of CdTe with no grain boundaries and CdTe with n-type doped grain boundaries (doped at $2.8 \cdot 10^{18}$ cm^{-3}) in a CdTe-CdS solar cell 46

List of Tables

Table 1. Materials parameters used in Afors-Het simulations 28

Table 2. Relaxation of epilayer determined from the reciprocal space maps. R.L.P. stands for reciprocal lattice points. Note that the relaxation of the (004) is not determined using this method 36

Acknowledgements

I would like to thank my thesis committee chair Dr. Xiangfeng Duan. I am thankful of Dr. Duan's support for me to pursue my master's degree.

I would also like to thank Dr. Alexander Spokoyny for serving on my thesis committee. I greatly appreciate his Chemistry 171: Intermediate Inorganic Chemistry course. His lectures set the foundation of my understanding of solid-state chemistry and have enabled me to pursue further studies in semiconductor physics successfully.

If it were not for Dr. Joseph DiStefano III's suggestion and encouragement, I would not have known about the Departmental Scholars Program. He has given me invaluable insight of how to approach research on a conceptual level. I have also had the honor to jam on jazz standards and practice classical etudes with Dr. DiStefano on both saxophone and flute.

I would like to acknowledge my first chemistry teacher Dr. James Drage for helping me discover my love for chemistry. Witnessing the violent reaction between sucrose and sulfuric acid inspired me to pursue chemistry. Prior to taking my first chemistry class, I planned on only becoming a professional musician. I am deeply grateful to Dr. Drage for helping me find a passion that I enjoy just as much as music.

My mother, grandmother, and grandfather have all supported me in my pursuit of my dreams. I am thankful for my grandparents' encouragement to pursue both chemistry and music. I am indescribably grateful to my mother for showing me how to persevere in life regardless of the obstacles I may face. She is a symbol of strength to me.

My colleagues were extremely helpful to me during this project. Chao Li and Ariella Machness have both helped train me on high-resolution x-ray diffraction. Without this characterization technique, analysis of the CdTe sample would have been nearly impossible.

I am extremely thankful to Dr. Yong-Hang Zhang and his students Calli Campbell and Cheng-Ying Tsai for providing high-quality CdTe grown on InSb. This project would have not been possible without their support.

I would like to thank my saxophone mentor Justo Almario. He has always fully supported both my musical and scientific endeavors. Having the chance to take private lessons with Professor Almario has allowed me to grow as a musician and as a human being. He has taught me the definition of a successful musician. Despite how hard life gets, Professor Almario has proved to me that being positive is the most important element of success.

And last, but not least, I want to thank Dr. Mark Goorsky for everything he has taught me. Not only has he given me the skills to be successful in the lab, but also what it takes to be a successful scientist. Dr. Goorsky has taught me how to analyze new information quickly and convey key points in a concise and meaningful manner to others. He has shown me the importance of how a scientist needs to be able to convince both scientists and non-scientists the importance of your own work and how it is relevant to everyone. Dr. Goorsky is the scientist I strive to emulate.

Chapter 1: Introduction

1.1 Motivation

Back in 1996, Loginov et al. [1] compared the efficiencies of polycrystalline CdTe-based solar cells before and after a $CdCl_2$ treatment. Their results showed that pre-$CdCl_2$ treated solar cells had an efficiency of 1.6% while post-$CdCl_2$ treated solar cells showed an efficiency of 10%. The most recent breakthrough was in 2015 when First Solar, Inc., produced a polycrystalline CdTe solar cell with an efficiency of 21.5% [2]. On the other hand, single crystalline CdTe solar cells have been shown to have an efficiency of 7.9% [3]. Polycrystalline CdTe has proven to be superior over its single crystalline counterpart. However, the exact mechanism of the $CdCl_2$ treatment is still not fully understood. Since one of the main differences between polycrystalline and single crystalline materials is the lack of grain boundaries in the latter, there is a notion that grain boundaries play a key role in the performance of $CdCl_2$-treated CdTe solar cells. The performance gap between these two forms of CdTe is intriguing because grain boundaries are, in general, detrimental to solar cell performance. Grain boundaries are understood to be charged-carrier traps and recombination centers that create a potential barrier at the region between two grains due to defects such as dangling chemical bonds [4]. Grain boundaries inhibit device performance by preventing electrical conduction. A visual depiction is shown in Figure 1.

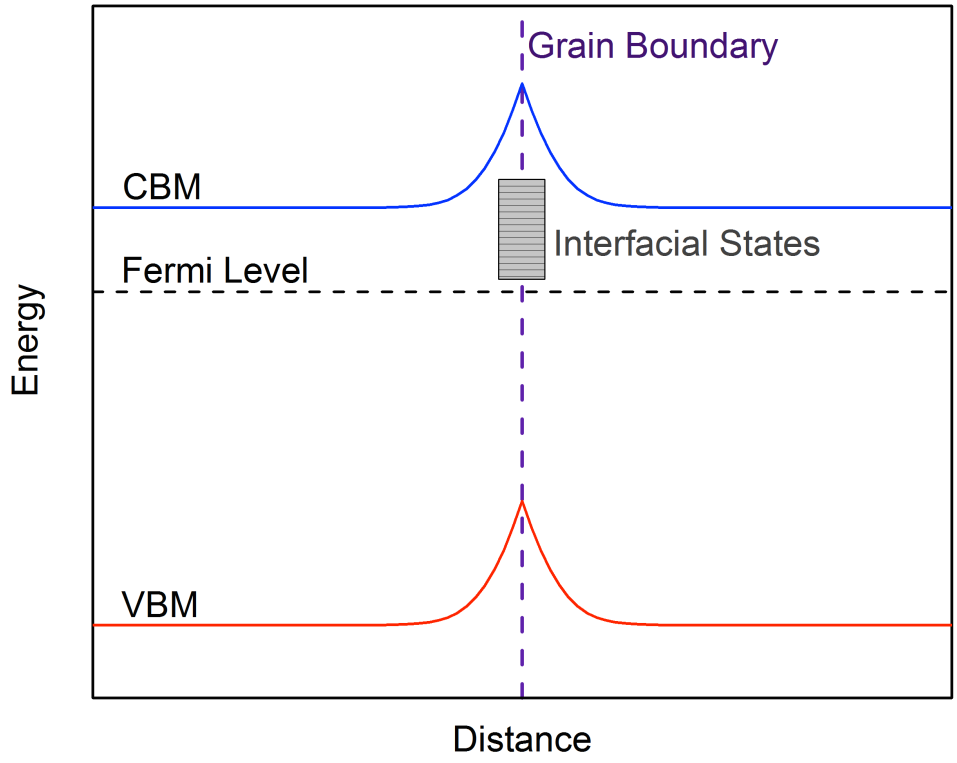

Figure 1. The energy profile of a grain boundary (vertical dotted line) for an n-type semiconductor. The interfacial energy states that capture majority carriers (electrons in this case) created by the grain boundary are represented by the gray box near the conduction band minimum (CBM). VBM stands for valence band maximum. Figure was inspired by Spencer et al. [5].

The $CdCl_2$ treatment is intended to remove this malignant property of grain boundaries. If this treatment makes the grain boundaries benign to device performance, then the efficiency of polycrystalline CdTe solar cells is expected to be less than or equal to its single crystalline counterpart and not an order of magnitude greater. For example, consider the differences between single crystalline and polycrystalline silicon solar cells. Single crystalline silicon solar cells are more efficient, but more expensive, than its polycrystalline form. On the other hand, polycrystalline silicon solar cells involve simpler processing methods than methods used to

fabricate single crystalline solar cells. There is a tradeoff between cost and device efficiency. The implication of polycrystalline CdTe's superiority over single crystalline CdTe is the potential to lower cost and increase efficiency simultaneously. Determining how the $CdCl_2$-treatment works in CdTe would impact our understanding of how to process other semiconductor materials.

One hypothesis of the $CdCl_2$ treatment's mechanism is it is simply a passivation process that lowers the harmful effects of grain boundaries by making them inert and reducing charged-carrier recombination [6]. A conflicting hypothesis suggests that the grain boundaries become n-type inverted post-$CdCl_2$ treated (note that the doping of CdTe in CdTe/CdS solar cells is p-type) and, as a result of this treatment, local p-n junctions are formed along the grain boundaries in CdTe [7]. These two ideas paint two different pictures for post-treatment CdTe: the former suggests an energy barrier depression while the latter suggests an energy barrier enhancement, as shown in Figure 2.

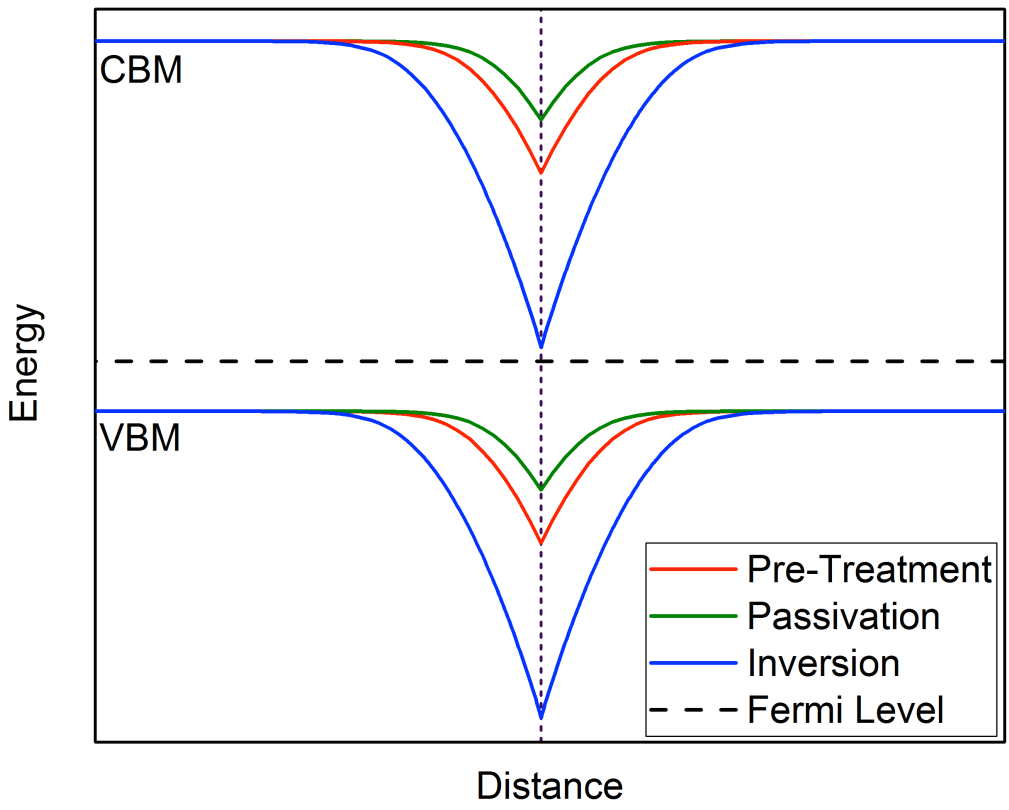

Figure 2. The energy profile of a grain boundary (vertical dotted line) in p-type CdTe. The median barrier (red) corresponds to a grain boundary before treatment. The smallest barrier (green) would occur if the $CdCl_2$ treatment passivates grain boundaries. The largest barrier (blue) would occur if the treatment inverts the grain boundary doping. Note that the Fermi level at the grain boundary is closer to the conduction band (n-type) while the Fermi level is closer to the valance band in the grain away from the boundary (p-type).

The justification for the local p-n junction hypothesis is C. Li et al. [7] reported observing that Cl atoms substitute Te atoms within a few unit cell distances from the grain boundary in sufficiently high enough concentrations to cause a local inversion from p-type to n-type only at the grain boundary. The conclusion is that grain boundaries can be altered to improve device performance by assisting in electron-hole separation and reduce electron-hole recombination.

Another observation supporting this hypothesis is a decrease in carrier recombination post-$CdCl_2$ treatment at the grain boundaries based off electron beam-induced current measurements. C. Li et al. also state that this effect is isotropic and grain boundary orientation is irrelevant. However, work done by H. Li et al. [4] classifies grain boundaries by orientation. H. Li et al. found that each type of grain boundary contributes differently to conduction after being treated with $CdCl_2$.

Despite the extensive amount of work done on polycrystalline CdTe, the mechanism of the $CdCl_2$ treatment and exact role of grain boundaries have yet to be comprehensively ascertained. Hence, direct wafer bonding of single crystalline CdTe wafers is an appealing approach since only one grain boundary is created at the bonded interface. Additionally, the orientation and surface chemistry of the interface (grain boundary) can be controlled. Sun et al. [8] have reported successfully bonding (111)-oriented CdTe wafers. However, no $CdCl_2$ treatment was done to their bonded samples.

The relevance of this preliminary study is to characterize single crystalline CdTe prior to direct wafer bonding. The CdTe used in this study have been grown on InSb substrates [9]. The surface roughness and strain of the CdTe is studied.

Chapter 2: Background and Theory

2.1 Atomic Force Microscopy

Atomic force microscopy (AFM) is an excellent tool for assessing surface roughness of materials. It is especially useful for direct-wafer-bonding applications since AFM can measure height at the nanometer resolution [10]. The basic principle of AFM is Hooke's law for springs: the force exerted on a spring is directly proportional to the spring's displacement from its equilibrium state [11]. The "spring" in AFM is a cantilever with a fine tip, whose tip size is typically less than 20 nm in diameter. The force is due to the interaction between the cantilever tip and a sample surface. The spring constant of typical cantilevers ranges from 0.01 to 50 N/m [12]. The cantilever is connected to a piezoelectric device, which is sensitive to mechanical forces exerted on the cantilever. A laser and photodiode is setup in order to monitor the cantilever, as shown in Figure 3.

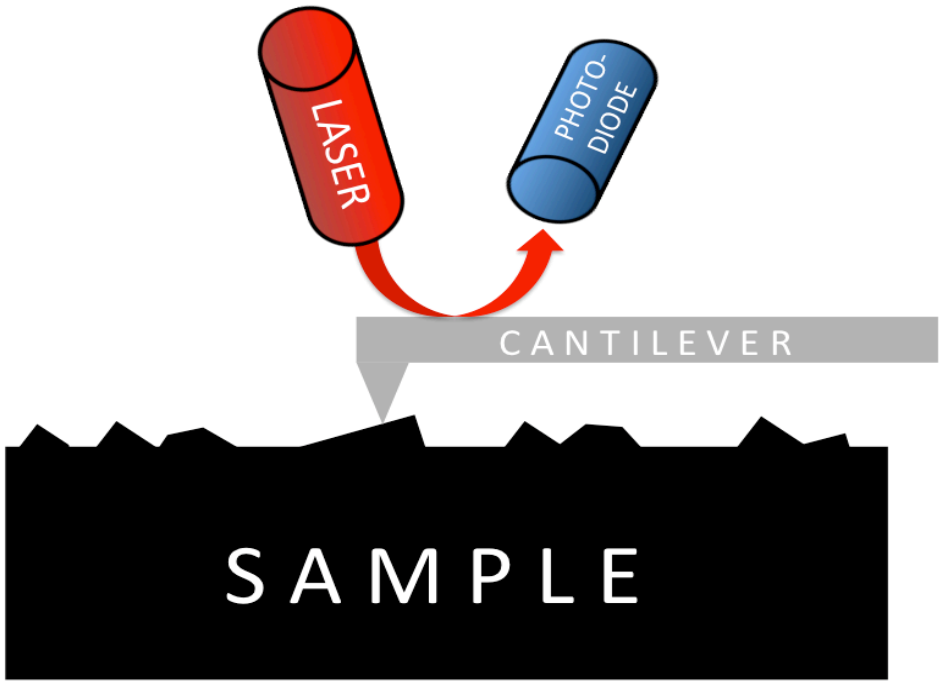

Figure 3. Schematic diagram of the AFM setup.

During each scan, the cantilever initially oscillates at its resonant frequency. As the cantilever tip moves along the sample surface, the tip is close enough to the surface such that van der Waals interactions is appreciable, i.e. attractive forces at relatively far distances and repulsive forces are close distances. As the tip encounters various surface topological features, the cantilever's frequency dampens. This dampening is detected by the laser-photodiode setup since the laser is reflecting off of the cantilever near the vicinity of the tip. When a decrease in frequency is detected, the height of the cantilever is adjusted in order to revert its frequency back to its original value; this adjustment is recorded as the height of a spot. An image of a sample surface can then be generated from the change in cantilever height with respect to in-plane surface location.

After probing the sample surface, the root mean square (RMS) of the sample surface topology is calculated and the resulting value interpreted as surface roughness, as shown in Equation 1 [13].

$$R = \sqrt{\frac{1}{L}\int_0^L \left| h(x)^2 \right| dx} \tag{1}$$

R is RMS roughness, h(x) is the measured surface height as a function of in-plane distance in the x-direction, and L is the length of the scan in the x-direction. RMS roughness is chosen to quantify surface roughness instead of arithmetic mean roughness because valleys and peaks, i.e. local extrema, influence RMS values more than they influence arithmetic mean values [14,15]. Thus, for applications such as direct wafer bonding of semiconductors, where sub-nanometer roughness is required for high-quality bonding, RMS values capture a better picture of surface roughness.

2.2 X-ray Diffraction and Reciprocal Space

X-rays can be used to nondestructively characterize materials by x-ray diffraction (XRD). XRD studies the relationship between diffraction peaks of crystallographic planes and angular displacements of those peaks, also known as Bragg's law. The underlying principle of Bragg's law is the phase relationship of waves. If waves are in-phase, then they reinforce each other and the path difference among the waves is an integer multiple of the wavelength. If waves are out-of-phase, then their amplitudes annihilate each other and the path difference among the waves is a factor of half-integer wavelengths [16].

At certain angles, x-ray beams aimed at a sample will interfere constructively and yield diffraction peaks while at other angles x-ray beams will interfere destructively and result in no peaks. To find the angles that correspond to diffraction peaks, consider Figure 4, which depicts

planes of atoms as horizontal dashed lines exposed to a beam of x-rays at an angle θ with respect to the atomic planes.

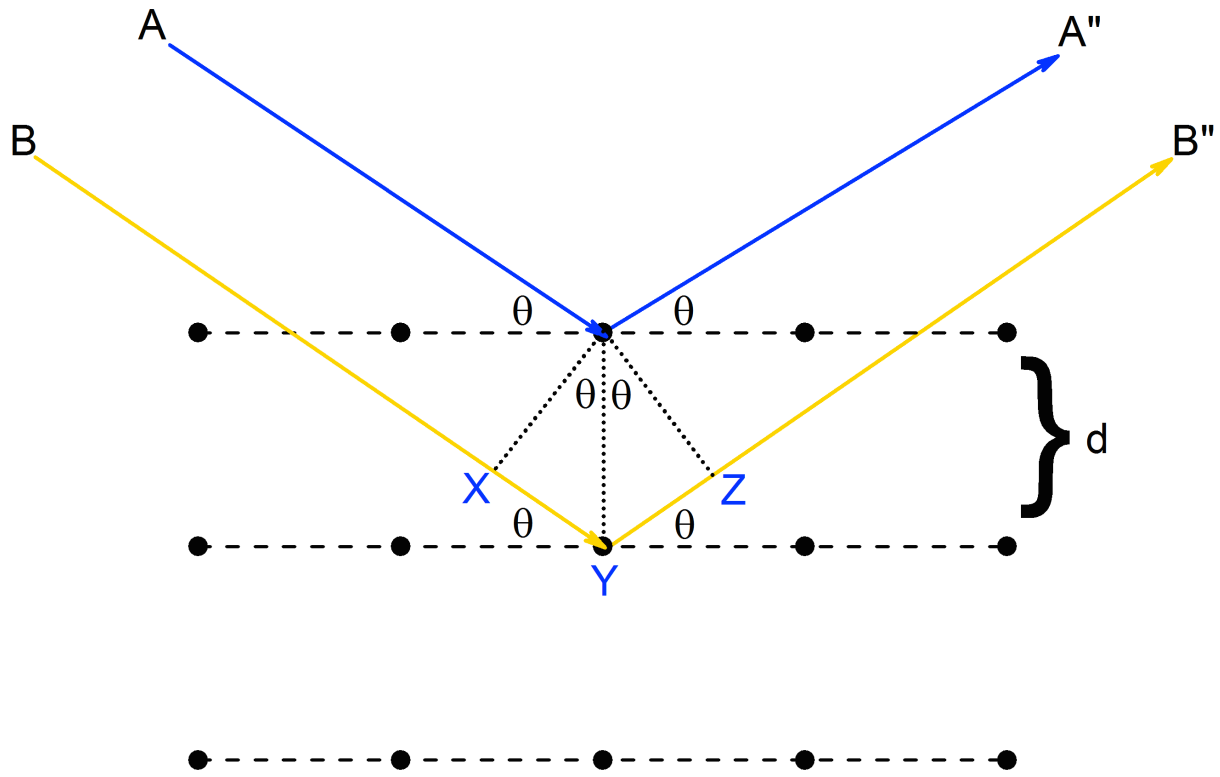

Figure 4. A schematic diagram of planes of atoms exposed to a beam of monochromatic x-rays.

Incident rays A and B are assumed to be parallel, i.e. the divergence angle between A and B is negligible, and they penetrate the surface at an angle θ. The exiting rays A" and B" also leave the surface at the same angle θ. From Figure 4 the path difference is:

$$XY + YZ = d\sin\theta + d\sin\theta \tag{2}$$

where d is the interplanar spacing between the atomic planes and XY and YZ are the path difference of A and B. For constructive interference to occur, the path difference between A and B must be an integer multiple of the x-ray wavelength:

$$XY + YZ = n\lambda \tag{3}$$

where n is an integer and λ is the x-ray wavelength. Combining Equation 2 with Equation 3 yields Bragg's law [17]:

$$n\lambda = 2d\sin\theta \tag{4}$$

Bragg's law states the relationship between wavelength, interplanar spacing, and diffraction angle (Bragg angle). For cubic systems, the relationship between d and lattice parameter is:

$$d = \frac{a}{\sqrt{h^2 + k^2 + l^2}} \tag{5}$$

where a is the lattice parameter of the material and h, k, and l are the Miller indices of a crystallographic plane.

The essential features of the XRD setup are shown in Figure 5.

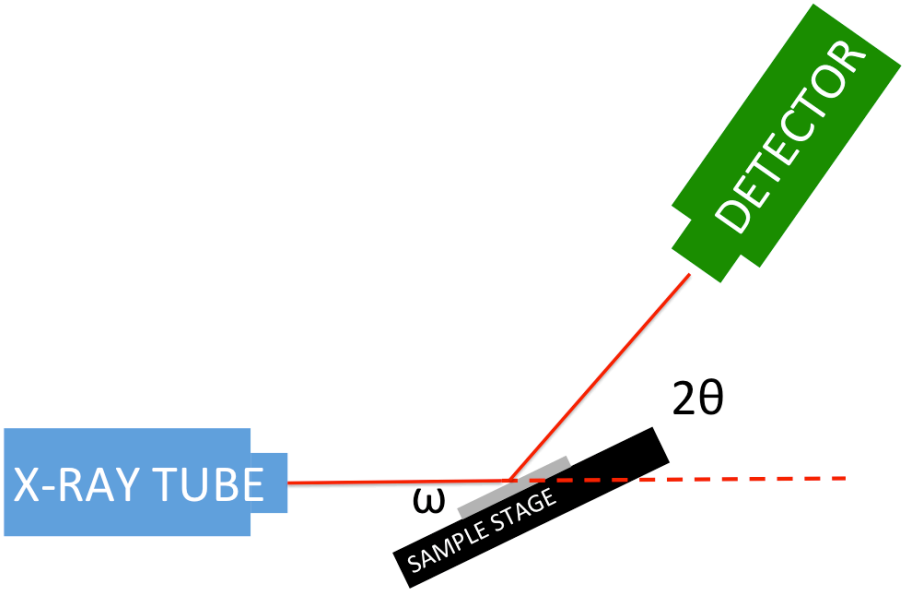

Figure 5. Schematic diagram of XRD. ω is the angle between the incident x-ray beam and the sample surface (thin gray block on sample stage). 2θ is the angle of the detector. This diagram depicts a symmetric scan.

The incident angle of the x-rays is ω while the angle of the detector is 2θ. In a symmetric ω:2θ scan, the ratio of ω to 2θ is 1:2. If the sample is polycrystalline, then all possible diffraction peaks can be observed in a symmetric scan. However, for single crystalline samples, the only possible peaks observable in symmetric scans are those corresponding to crystallographic planes parallel to the sample surface. However, other crystallographic planes can still be observed by taking asymmetric scans called glancing incidence (G.I.) and glancing exit (G.E.) scans. G.I. and G.E. scans can access planes other than those orientated parallel to the sample surface by adjusting ω from the Bragg angle, θ_B, by an angle $\pm\varphi$, where φ is the angle between the surface plane and the desired crystallographic plane.

$$\omega = \begin{cases} \theta_B - \varphi, & for \quad G.I. \\ \theta_B + \varphi, & for \quad G.E. \end{cases} \tag{6}$$

Figure 6 and Figure 7 depict G.I. and G.E., respectively.

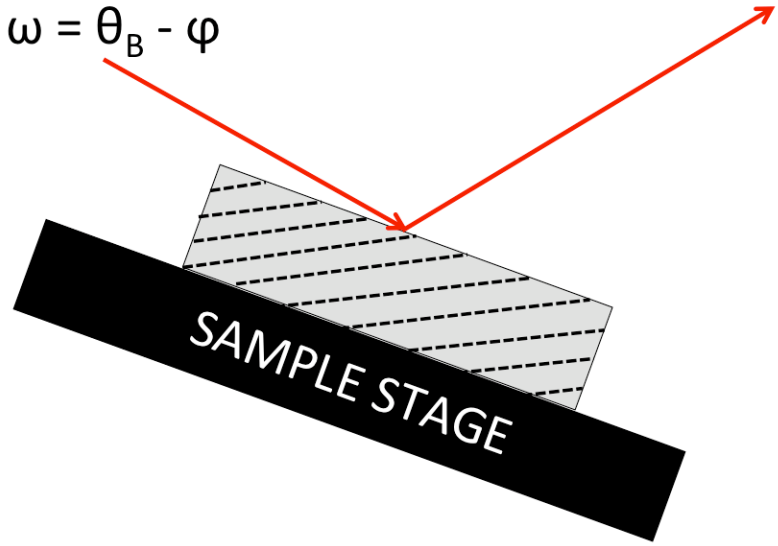

Figure 6. Schematic diagram of the glancing incidence asymmetric scan. The dashed lines represent the crystallographic planes nonparallel to the sample surface that are inaccessible by symmetric scans.

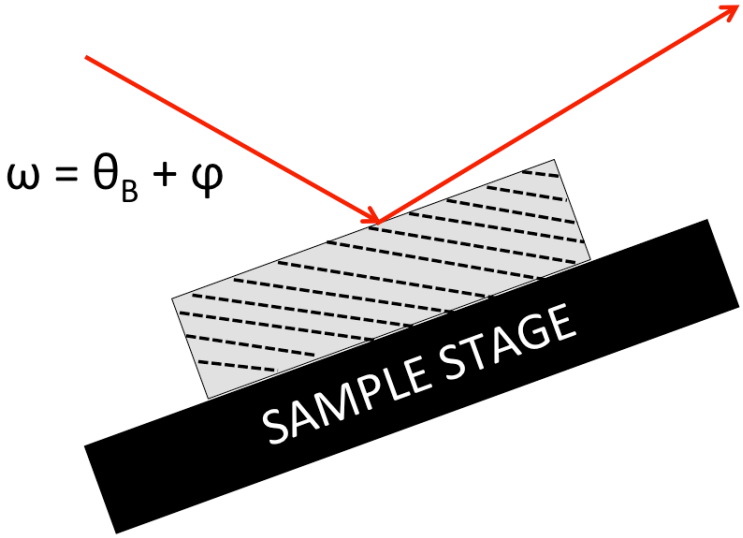

Figure 7. Schematic diagram of the glancing exit asymmetric scan. The dashed lines represent the crystallographic planes nonparallel to the sample surface that are inaccessible by symmetric scans.

Note that in G.I. the outgoing rays are much broader than the outgoing rays in G.E. due to its wide exiting range. Consequently, the resolution for G.I. is worse than the resolution of G.E. because G.I. has a wider range of maximum intensity values than G.E. does. For this reason, G.E. is used to make reciprocal space maps instead of G.I.

Mapping out crystallographic planes in reciprocal space can be done using high-resolution x-ray diffraction (HRXRD) [18]. In reciprocal space, analysis is done with the reciprocal values of direct space values. It should be noted that interplanar angles and crystal structures are not affected by reciprocal space transformations; all symmetry features are conserved. Reciprocal space is a convenient way of mapping out crystallographic planes as single reciprocal lattice points. While the reciprocal space points of all the crystallographic planes reside in 3 dimensions, the reciprocal space maps generated using HRXRD are two-dimensional projections of reciprocal space [16]. Each projection is defined by two crystallographic directions called zone axes.

Not all crystallographic planes can be mapped out using HRXRD due to diffractometer limitations. The limiting sphere, whose radius is twice the reciprocal of the x-ray wavelength, is a boundary for which planes found outside this sphere cannot be measured since Bragg's law is invalid for sine values greater than 1. Additionally, some planes will not be obtainable even if they lie within the limiting sphere in reciprocal space because these planes lie in a region called the transmission geometry region. Planes inside this region require angles of incidence and angles of exit less than zero [18]. So planes such as (111) and (422) of CdTe for a (001)-oriented CdTe layer will not be accessible under the experimental conditions of this work, as shown in Figure 8. Each transmission geometry region is spanned by a sphere whose radius is the reciprocal of the x-ray wavelength.

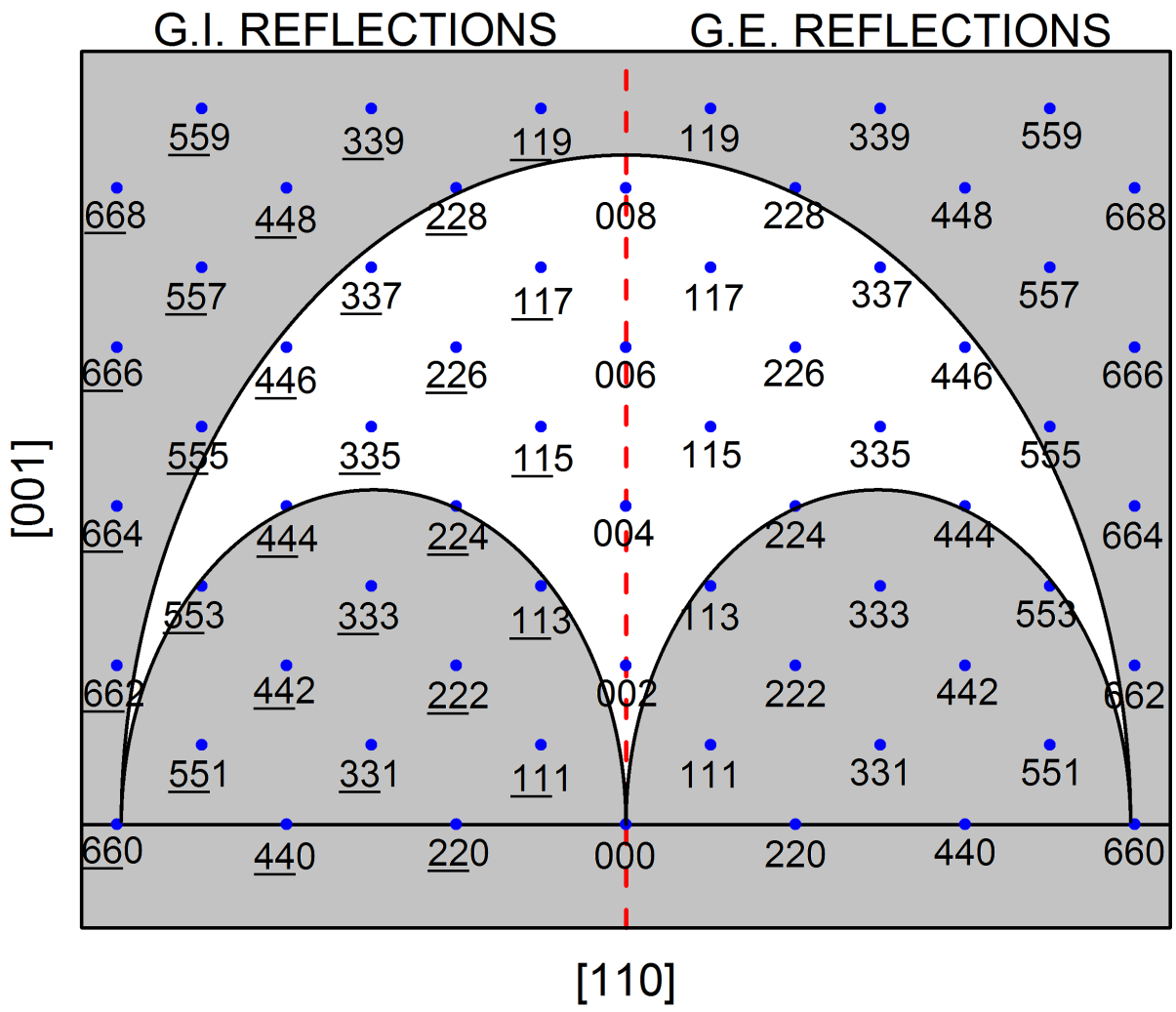

Figure 8. A scaled reciprocal space map sketch for CdTe. Inaccessible planes are those in the shaded gray regions. The x-ray wavelength used is Cu $K\alpha_1$, which is 1.54056 Å [16]. Note that planes accessible to G.E. scans are planes along the positive (right) side of the [110] zone axis and planes accessible to G.I. are found on the negative (left) side of this axis. Symmetric scans follow the vertical dashed line along the [001] direction.

Note that the lattice parameters of CdTe and InSb are 6.482 Å [19,20] and 6.47937 Å [21], respectively. Thus, along the [001] zone axis the InSb reciprocal lattice points would be slightly above the CdTe points. Along the [110] zone axis the InSb points would be slightly

further away from the origin than the CdTe points. Since the lattice parameters differ by 0.04%, the peaks are not distinguishable on the scale used in Figure 8.

It is important to realize that any rotation in direct space is translated directly into the rotation in reciprocal space. That means however a sample is rotated, its reciprocal lattice points also follow that same rotation. These rotations are controlled by angles ϕ and χ in the x-ray diffractometer, as shown in Figure 9.

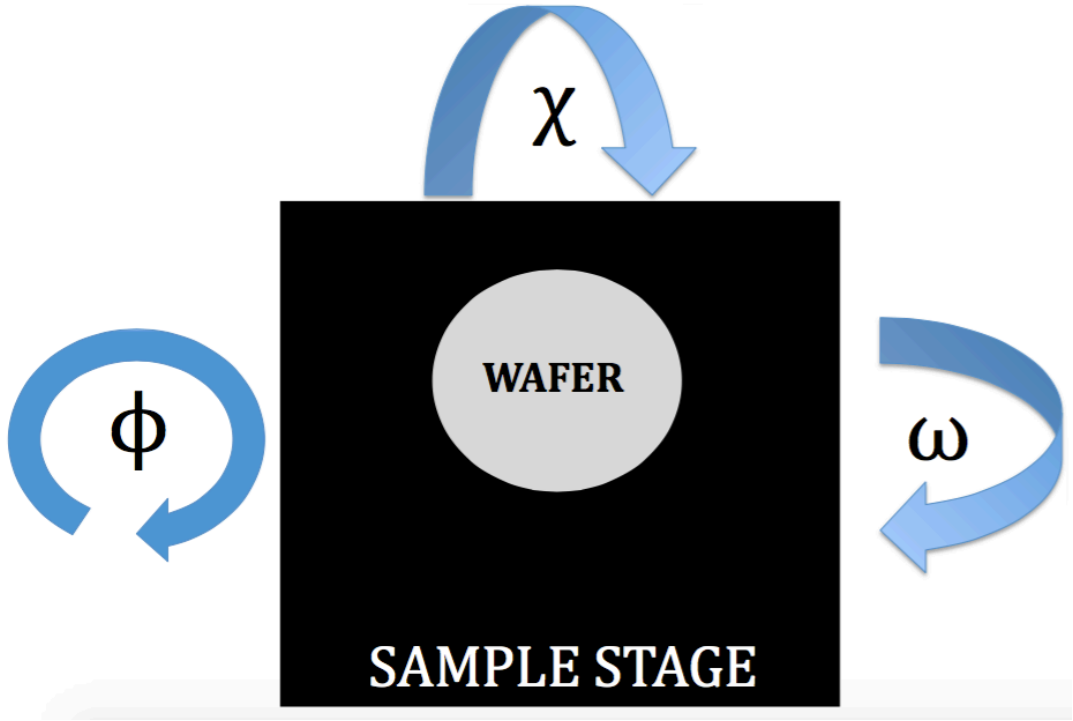

Figure 9. Angles ϕ and χ correspond to in-plane rotation and out-of-plane rotation, respectively. ω is shown as a point of reference from Figure 5.

ϕ is the in-plane rotation angle whose axis of rotation comes out of the page, while χ is like ω but with its axis of rotation oriented horizontally along the dimension of the page (e.g. rotating χ in the positive direction causes the top of the sample stage to come out of the page while the bottom

of the stage moves into the page). Controlling ϕ and χ is important because reciprocal space maps of different crystallographic planes can only be directly compared with each other if they are on the same two-dimensional projection. In other words, manipulating ϕ and χ properly allows, in the case of this study, both the [001] and [110] poles to align in the diffraction plane to eliminate any misorientation-induced artifacts into the reciprocal space map. Previous work done by Lam [22] has shown that in order to align the proper zone axes for each diffraction plane, these planes must share ϕ and χ values.

The material used in this study is CdTe epitaxially grown on an (001) InSb substrate. The crystalline substrate can be thought of as a template wafer that functions as a seed crystal for which the deposited epilayer binds into one or more crystallographic orientations with respect to the substrate [23]. In the case of this work, the substrate-epilayer interface consists of the (001) plane of the substrate bound to the (001) plane of the epilayer. Since the epilayer and substrate are different materials, the difference in lattice parameters between the materials plays an important role in the amount of strain and distortion induced in the epilayer. In the case of CdTe grown on InSb, the lattice mismatch between these materials is 0.04%; compared to other studies of CdTe grown on GaAs [24] or Si [25] where the lattice mismatch is 14.7% and 19.35%, respectively. The strain on the epilayer can be discussed in terms of relaxation [18] as shown in Equation 7.

$$R = \frac{a_{=} - a_s}{a_{x,R} - a_s} \tag{7}$$

R is relaxation, $a_{=}$ is the strained in-plane (along the surface of the substrate) lattice parameter of the epilayer due to the substrate, a_s is the substrate lattice parameter, and $a_{x,R}$ is the in-plane intrinsic lattice parameter of the epilayer. Relaxation ranges from 0% to 100% and is depicted in Figure 10.

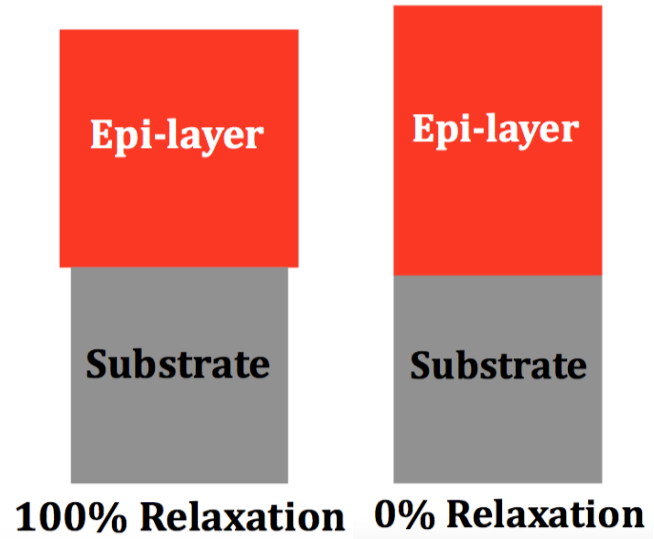

Figure 10. 100% relaxation (left) is the case where the epilayer is not strained at all by the substrate and is therefore not distorted. 0% relaxation (right) corresponds to a tetragonally distorted epilayer where the in-plane lattice parameter shrinks while the out-of-plane lattice parameter expands.

The case of 0% relaxation is an example of a coherent or pseudomorphic layer. When the epilayer is only partially strained or relaxed the result is an incoherent layer. In the case of 100% relaxation, the in-plane lattice parameter is the same as the epilayer's intrinsic value. This occurs when the epilayer becomes greater than the critical thickness allowed by the epilayer-substrate system [23].

Lastly, for biaxially strained (001) oriented layers, the relationship between distorted out-of-plane and in-plane lattice parameters is shown in Equation 8 [18].

$$\frac{a_{e,relaxed}-a_s}{a_s}=\left(\frac{1-\upsilon_e}{1+\upsilon_e}\right)\cdot\left(\frac{a_\perp-a_s}{a_s}\right)+\left(\frac{2\upsilon_e}{1+\upsilon_e}\right)\cdot\left(\frac{a_=-a_s}{a_s}\right) \tag{8}$$

$a_{e,relaxed}$ is the epilayer material's intrinsic lattice parameter, a_s is the substrate lattice parameter, υ_e is the Poisson ratio of the epilayer, $a_\perp$ is the strained out-of-plane (normal is substrate

surface) epilayer lattice parameter, and $a_{=}$ is the strained in-plane epilayer lattice parameter. This equation can be rewritten so that relaxation is in terms of these variables, as shown in Equation 9.

$$R = \left[1 - \left(\frac{1-\upsilon_e}{1+\upsilon_e}\right) \cdot \left(\frac{a_{\perp} - a_s}{a_{e,relaxed} - a_s}\right)\right] \cdot \left(\frac{1+\upsilon_e}{2\upsilon_e}\right) \tag{9}$$

2.3 Semiconductors and p-n Junctions

In band theory, the energy profile of semiconductors is depicted by two bands called the valance band and conduction band, which are separated by an energy distance corresponding to a semiconductor's band gap. This band gap region is also known as the forbidden region. To graphically distinguish between undoped and doped semiconductors, consider the relative location of the Fermi level. In intrinsic semiconductors (pure semiconductors with a negligible impurity concentration), the Fermi level is found in the middle of the band gap. In extrinsic semiconductors (semiconductors intentionally doped with impurities), the Fermi level of n-type (mobile-electron rich) materials is found near the conduction band minimum while in p-type (mobile-hole rich) materials it is found near the valence band maximum [26], as shown in Figure 11.

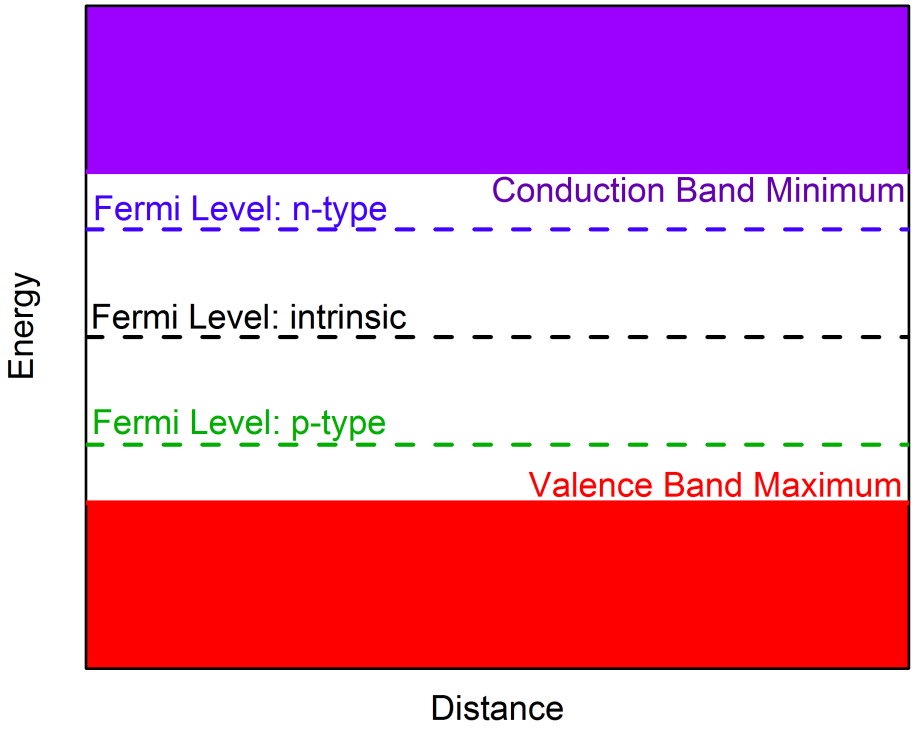

Figure 11. Schematic band diagram of intrinsic and extrinsic semiconductors. The shaded purple (top) region is the conduction band and the shaded red (bottom) region is the valance band.

How close the Fermi level is to the valance band maximum or conduction band minimum for p-type and n-type materials, respectively, depends on the impurity atom's ionization energy. The easier a dopant atom ionizes, the closer the Fermi level is to the host semiconductor's valance band maximum/conduction band minimum. This is under the assumption that the semiconductor remains a nondegenerate semiconductor after doping. A nondegenerate semiconductor is doped at concentrations such that the Fermi level does not rise above the conduction band minimum or fall below the valance band maximum. Otherwise, semiconductors doped at sufficiently high enough impurity concentrations such that the Fermi level falls outside the forbidden region are called degenerate semiconductors [26].

Now suppose the semiconductor in Figure 11 is placed under bias; this causes the band diagram to tilt downwards from the positive end to the negative end of the bias [27], as shown in Figure 12.

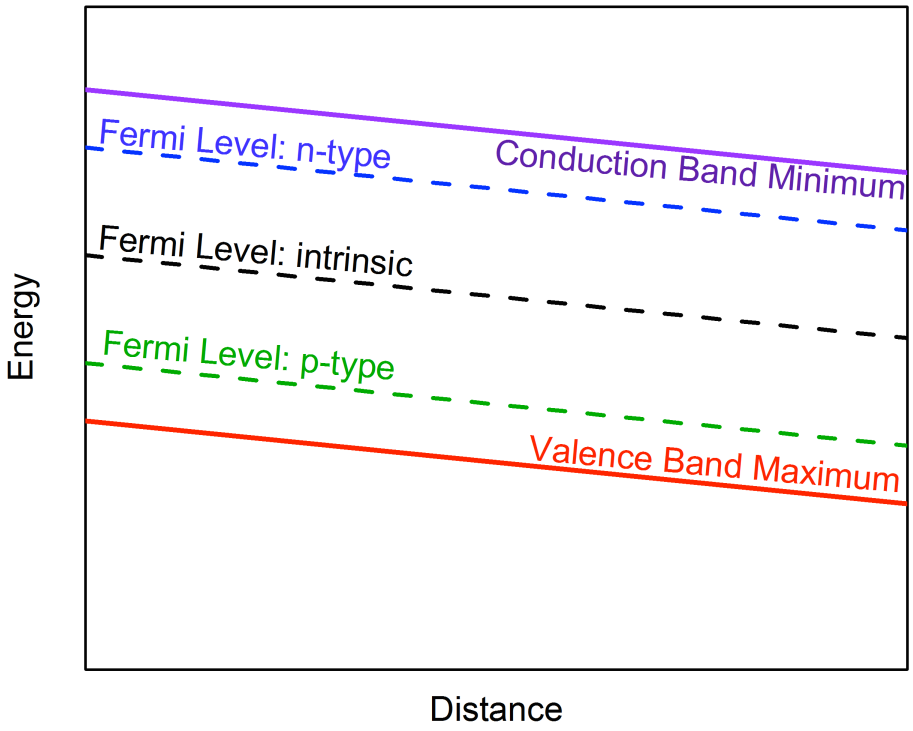

Figure 12. The band diagram of the semiconductor from Figure 11 placed under bias. The positive end of the bias is on the left side of the band diagram.

The energy difference between each end (left and right boundaries of Figure 12) of the energy levels corresponds to the amount of applied bias and the slope of the energy levels corresponds to the force experienced by charged carriers conducting through the semiconductor [27].

Solar cells are fundamentally made of an n-type and a p-type material joined together to form a p-n junction. In terms of band theory, when an n-type and a p-type material are brought

together to form a junction, each material's Fermi level must be matched. Thus, at the junction, a smooth intermediate region must connect the conduction band minimum and valance band maximum of each material together; the energy bands of each material are not connected by a disjointed step [28]. This is shown in Figure 13 and Figure 14. The intermediate region is known as the depletion region or space-charge region because density of mobile charged carriers is zero as a result of the interaction between the n-type and p-type materials' dopant species during the formation of the p-n junction [29,30].

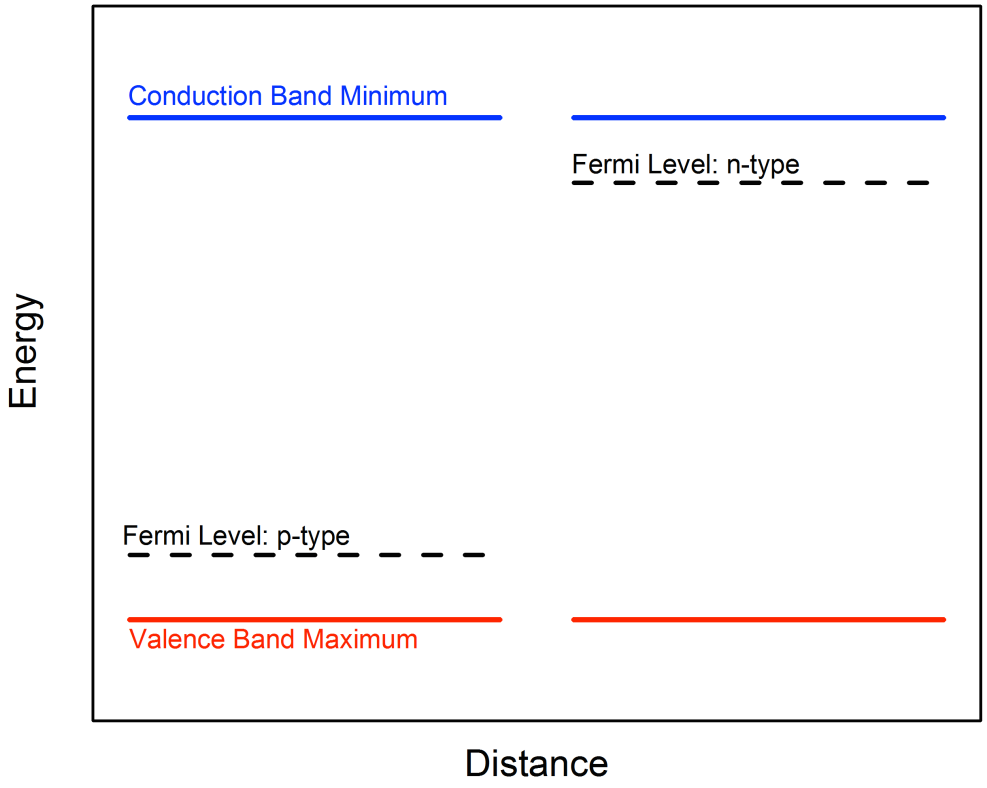

Figure 13. A p-type and an n-type semiconductor prior to forming a p-n junction.

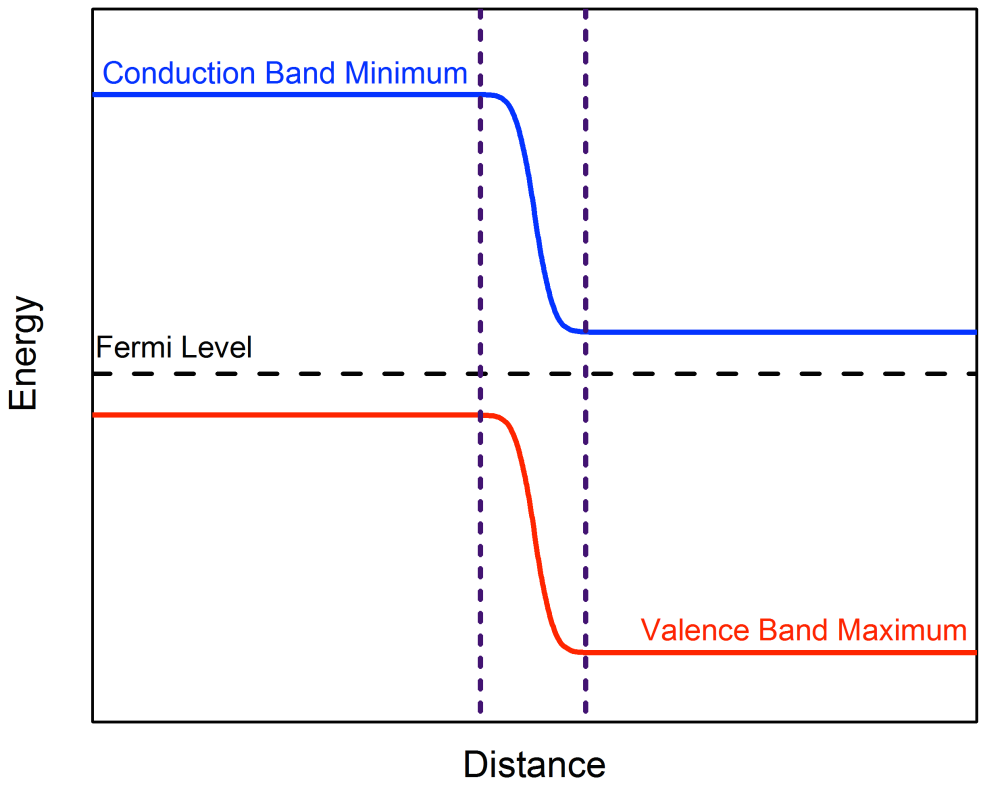

Figure 14. Band diagram of a p-n junction. Vertical dotted lines indicate the depletion region width.

Chapter 3: Experiment

A sample of (001) CdTe film grown on an (001) InSb substrate via molecular beam epitaxy [9] is studied. The amount of possible unintentional miscut is ±0.1˚ and the CdTe layer is undoped.

3.1 AFM: Surface Roughness and Stacking Fault Analysis

The surface of CdTe grown on InSb is studied using a Quesant Q-Scope 250 AFM. Each scan is done at the equipment's maximum scanning limits: 40 μm by 40 μm scanning area. First, the surface roughness is measured. Stacking faults are observed on all 40 μm by 40 μm scans. The dimensions of the stacking faults are measured and used to calculate the thickness of the grown CdTe layer by considering the interplanar angle between the CdTe's surface orientation and the (111) plane.

3.2 High-resolution X-ray Diffraction and Reciprocal Space Maps

Reciprocal space maps are generated using high-resolution x-ray diffraction to study the amount of relaxation of the CdTe layer grown on an (001) InSb substrate. The equipment used is a Bede D1 high-resolution diffractometer capable of performing both double-axis diffraction (DAD) and triple-axis diffraction (TAD). The diffractometer uses a copper x-ray tube source. The schematic setup is shown in Figure 15.

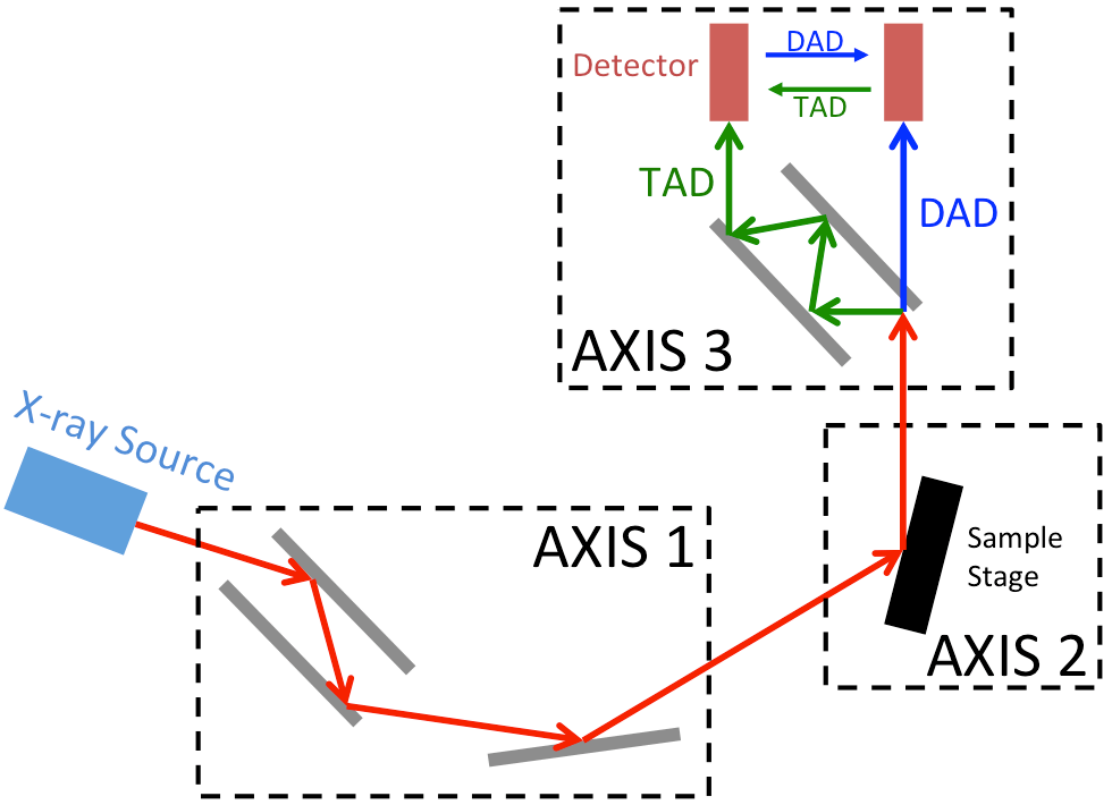

Figure 15. Schematic diagram of the high-resolution x-ray diffractometer used. Axis 1 is a beam conditioner that consists of a 3-bounce channel cut (111) silicon monochromator. Axis 2 is the sample stage (ω). Axis 3 is the detector and analyzer crystal; the analyzer crystal is a 4-bounce (220) channel cut silicon used to enhance resolution for TAD. For DAD, the crystal is moved out of the way of the x-ray beam.

Axis 1 consists of a three-bounce channel cut (111) silicon crystal used as a monochromator. Axis 2 contains only the sample stage. For DAD, only a narrow slit is used in front of the detector; while for TAD, a third crystal (analyzer crystal, four-bounce (220) channel cut silicon) is also used to enhance resolution. Note that because of Axis 1, the diffractometer is able to selectively pick out, to a very good approximation, just the Cu $K\alpha_1$ wavelength (1.54056 Å) from the x-ray source. This is necessary since the generation of x-rays produces not just one

wavelength of x-ray, but a continuous spectrum of x-rays [32]. TAD is used only for generating the (004) reciprocal space map while DAD is used to generate the (115) and (335) reciprocal space maps.

To generate reciprocal space maps, multiple ω:2θ scans are measured while stepping along ω after each ω:2θ scan. For example, the first scan for the (004) reciprocal space map is an ω:2θ scan at ω = -500 arcseconds; then, the next ω:2θ scan is done at ω = -490 arcseconds, and so on. This works because ω:2θ scans trace out straight lines in reciprocal space emanating from the reciprocal space origin and ω traces out arcs in the direction orthogonal to the ω:2θ scan.

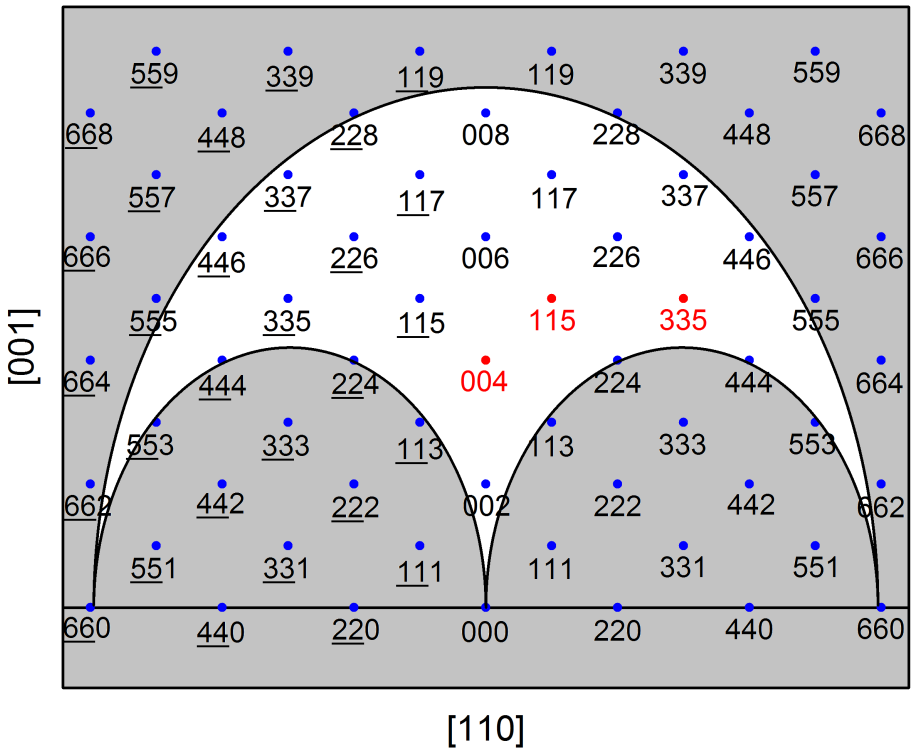

Figure 16: Reciprocal space maps are generated for the (004), (115), and (335) peaks.

Additionally, the angles ϕ and χ (see Figure 9) used are such that the ϕ and χ values are shared between the symmetric scan and asymmetric scans in order to ensure both the [001] and [110] poles align in these diffraction planes.

After generating the maps, a simulation program called Rocking Curve Analysis by Dynamical Simulation (RADS) created by Bede Scientific is used to correlate relaxation (see Equation 7 and 9) with diffraction peak separation of the CdTe epilayer and InSb substrate diffraction peaks. Experimental rocking curves are then compared with the theoretical calculations from RADS.

3.3 Heterojunction Simulation

Automat for Simulation of Heterostructures (Afors-Het, v.2.4.1) [33] is a simulation program for semiconductor materials. Under the premise of the local p-n junction hypothesis [7], Figure 17 depicts the structure used in Afors-Het.

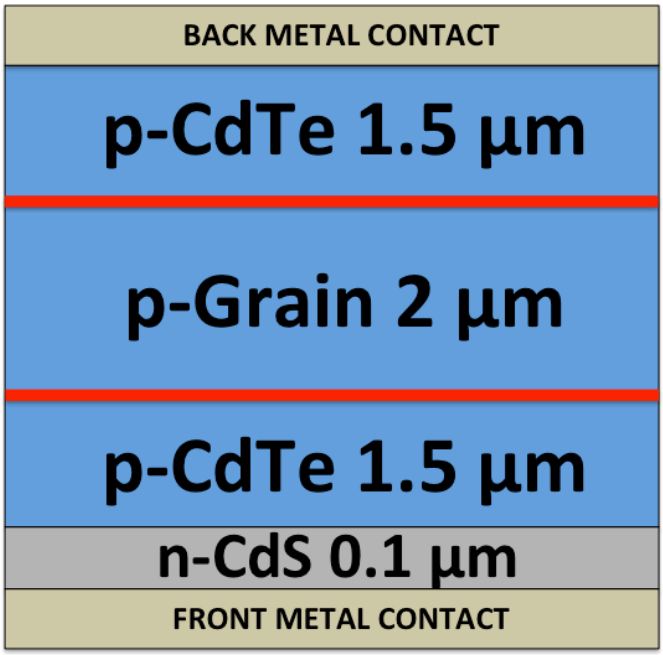

Figure 17. Structure used in Afors-Het. The grain boundaries are represented by red lines and are doped n-type. The bulk and grain of CdTe are both p-type and the CdS layer is n-type.

The grain boundaries are assumed to undergo n-type inversion due to a $CdCl_2$ treatment [7]. The red lines represent 1-nm grain boundaries [34] and the n-type doping concentration of the grain boundaries is varied. Both grain boundaries are doped equally. The CdTe is doped 10^{15} cm^{-3} p-type [35] and the CdS is doped 10^{17} cm^{-3} n-type [36]. The CdTe and CdS are 5 µm and 0.1 µm, respectively [37]. The grain is given a width of 2 µm. The energy profile is then generated by Afors-Het. The materials parameters used are summarized in Table 1.

	CdTe	**CdS**
Dielectric Constant (Static, Low Frequency)	10.2 [38]	10. [36]
Electron Affinity (eV)	4.28 [39]	4.0 [40]
Band Gap (eV)	1.45 [38]	2.42 [38]
Effective Conduction Band Density of States (cm^{-3})	$8 \cdot 10^{17}$ [36]	$2.2 \cdot 10^{18}$ [36]
Effective Valence Band Density of States (cm^{-3})	$1.8 \cdot 10^{19}$ [36]	$1.8 \cdot 10^{19}$ [36]
Electron Mobility $(cm^2 \cdot V^{-1} \cdot s^{-1})$	1050 [38]	340 [38]
Hole Mobility $(cm^2 \cdot V^{-1} \cdot s^{-1})$	100 [38]	340 [38]

Table 1. Materials parameters used in Afors-Het simulations.

Chapter 4: Results and Discussion

4.1 AFM Results

A picture of the sample is shown in Figure 18. Five AFM scans evenly spread out over the sample were measured and the result for one spot is shown in Figure 19. Each scan showed similar results with each other.

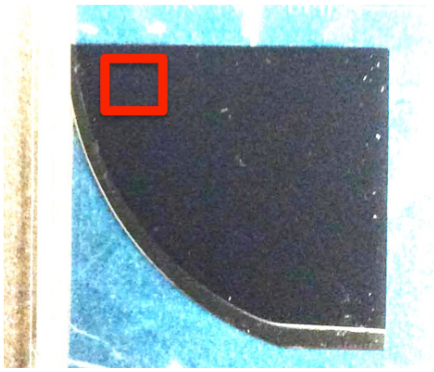

Figure 18. The CdTe on InSb sample used in this study. The CdTe epilayer is the black region and the silver border at the CdTe's periphery is the exposed InSb substrate beneath the epilayer. The red square indicates the region of one of the five scans measured corresponding to Figure 19. The sample is 2.5 cm on edge.

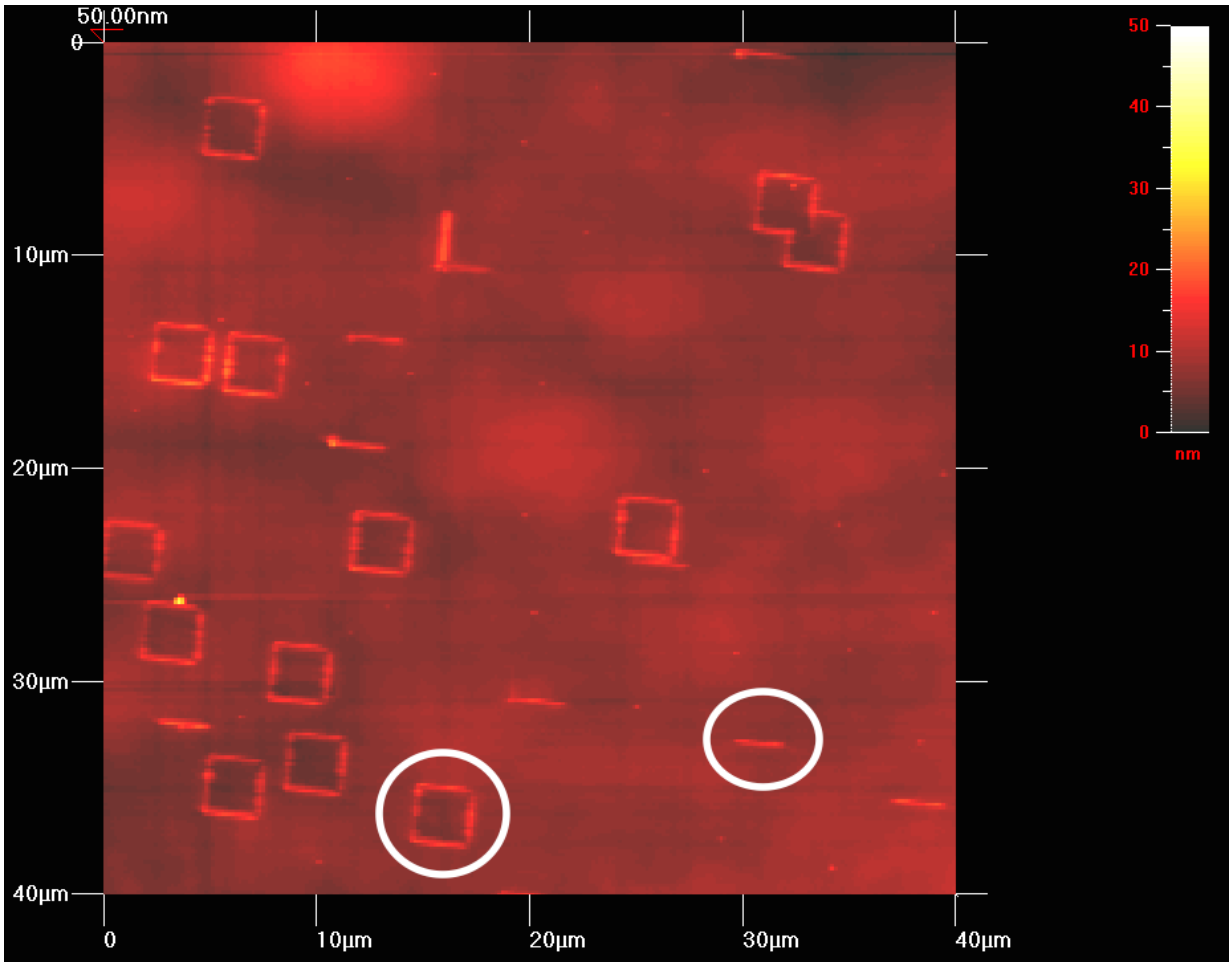

Figure 19. 40 µm by 40 µm AFM scan within the region indicated in Figure 18. The squares and lines (examples are circled in white) are stacking faults. The average RMS smoothness of regions outside the stacking faults is 0.9 nm.

The squares and lines observed in the AFM scans are stacking faults most likely caused by oxide patches on the sample surface present during epitaxial growth. Finch et al. [41] showed if patches of oxide are present on single crystal silicon, it is common for stacking faults to grow on four {111} planes and form square structures (note that braces refer to crystallographic planes within the same family while parentheses indicate a single plane) on (001)-oriented silicon. They

also show that another common stacking fault structure is a linear, rectangular structure. These are observed in Figure 19 as the lines that are about the same width as the squares. Even though Finch et al. studied silicon, the same concepts still apply to CdTe because both materials share the same crystal structures.

Since the surface structures in the AFM scans are stacking faults on the {111} planes, the thickness of the CdTe epilayer can be calculated. Consider the schematic profile of a square stacking fault shown in Figure 20.

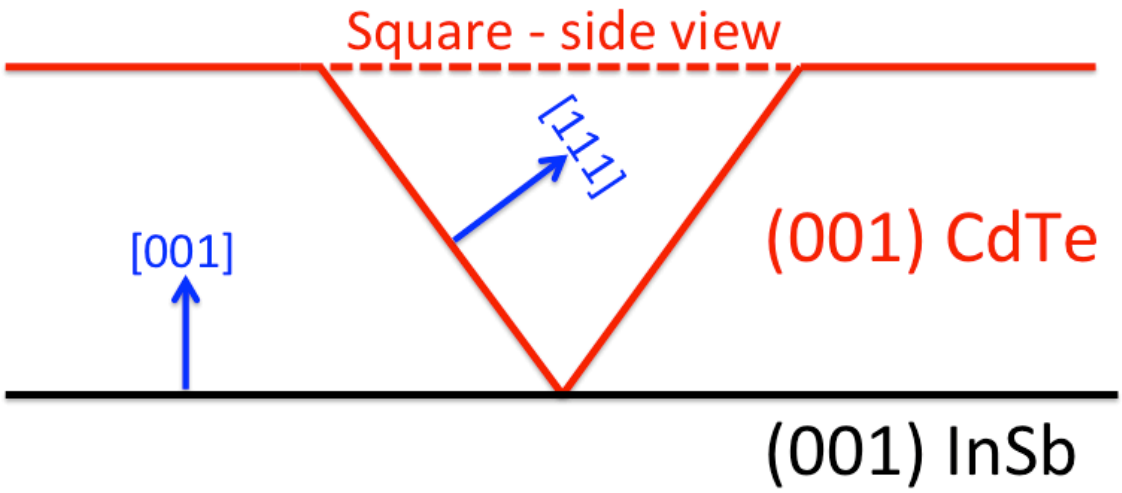

Figure 20. Schematic side profile of the square stacking faults on the CdTe epilayer. Note that crystallographic directions (vectors) are indicated in square brackets. These directions are orthogonal to their respective crystallographic planes, e.g. [001] direction is normal to the (001) plane [43].

The angle between two planes can be calculated by evaluating the dot product between the vectors orthogonal to each plane [42]. The angle between the (001) and (111) plane is 54.74˚.

Using trigonometry, the thickness of the CdTe layer can be determined from this interplanar angle and the width of the square stacking fault, as calculated in Equation 10.

$$Thickness = \left(\frac{1}{2} \cdot SquareWidth\right) \cdot \tan\left(54.74°\right) \tag{10a}$$

$$Thickness = \left(\frac{1}{2} \cdot 2.6\mu m\right) \cdot \tan\left(54.74°\right) \tag{10b}$$

$$Thickness = 1.8\mu m \tag{10b}$$

The thickness of the CdTe epilayer is assessed to be 1.8 μm thick.

The roughness of the regions outside the stacking faults was also measured. The average RMS roughness turns out to be 0.9 nm, a value suitable for direct wafer bonding applications. However, direct wafer bonding of the CdTe sample in its current condition will prove to be fruitless. Direct wafer bonding requires smooth surfaces and topological features like stacking faults will inhibit high-quality bonding results [31]. A controllable process to remove stacking faults needs to be developed.

4.2 HRXRD Results

The reciprocal maps of the (115), (004), and (335) CdTe and InSb peaks are shown in Figure 21, Figure 22, and Figure 23, respectively. Note that all these maps are placed on the same length scale.

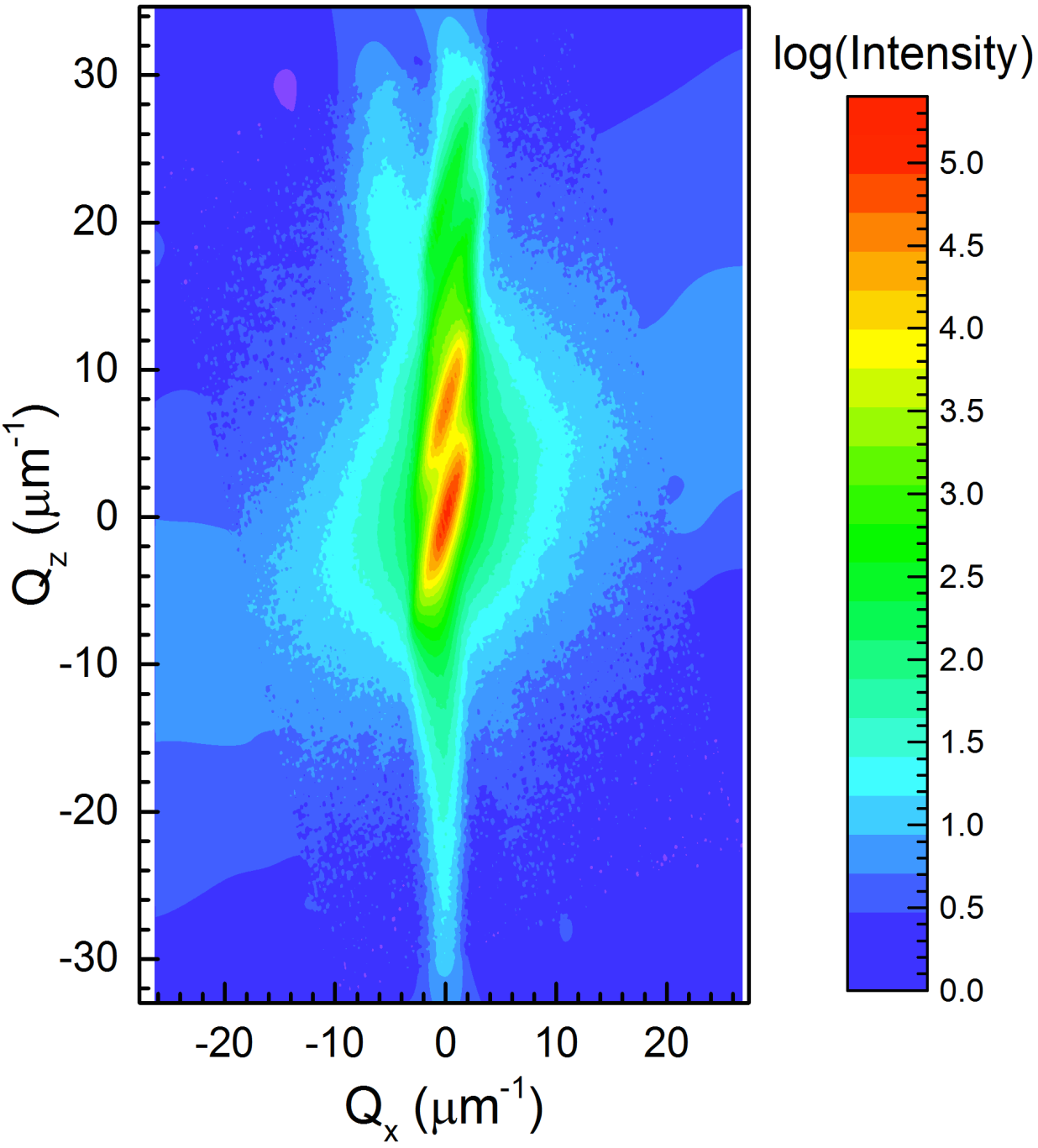

Figure 21. Reciprocal space map of the (115) peaks. This map is on the same length scales as the other reciprocal space maps in Figure 22 and Figure 23.

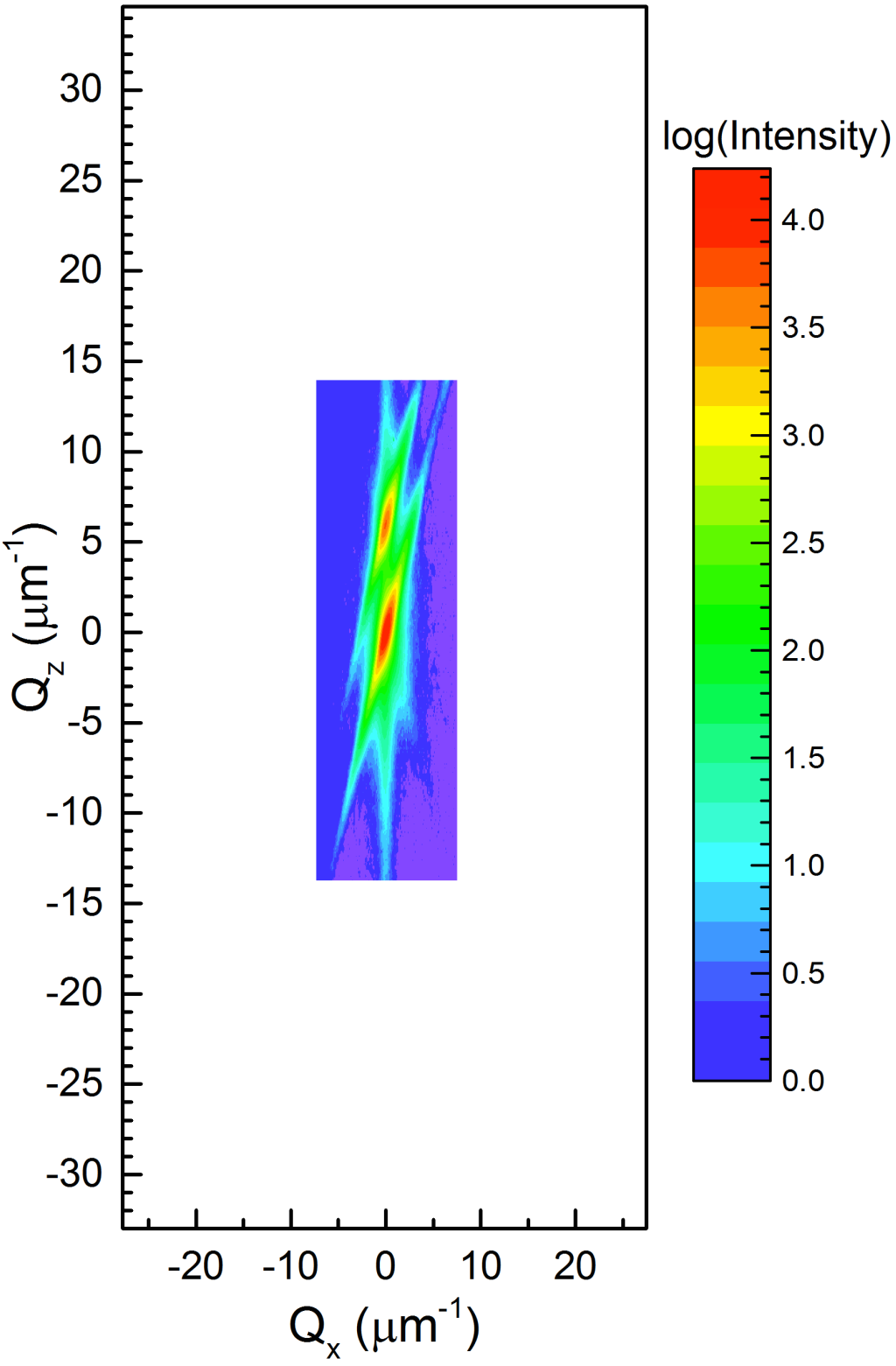

Figure 22. Reciprocal space map of the (004) peaks. This map is on the same length scales as the other reciprocal space maps in Figure 21 and Figure 23.

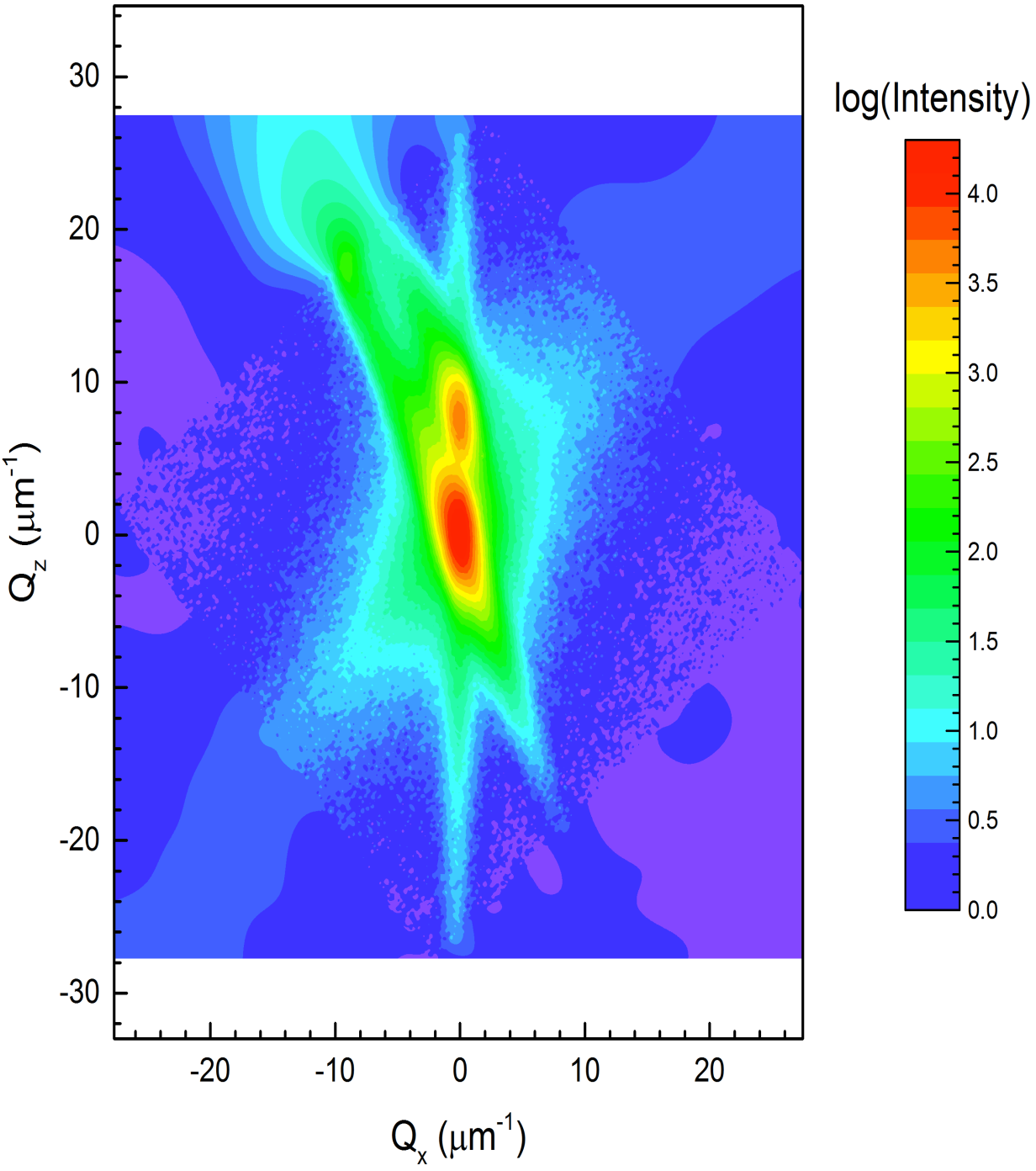

Figure 23. Reciprocal space map of the (335) peaks. This map is on the same length scales as the other reciprocal space maps in Figure 21 and Figure 22.

The streaks observed in the reciprocal space maps are due to x-ray scattering of the sample and the fact that the diffractometer has a finite angular resolution [44].

The amount of relaxation of the CdTe epilayer on the InSb substrate can be ascertained from these reciprocal maps. First the angle between the CdTe and InSb reciprocal lattice points (point of maximum intensity) and direction normal to the map (Q_z direction) is calculated. This is done by taking one of the lattice points as a reference point and determining the coordinates of a vector that joins both reciprocal lattice points. The dot product of this vector and a vector along the Q_z direction is evaluated to determine the angle between these vectors. Then, the interplanar angle between the crystallographic plane of interest and epilayer surface orientation is calculated. The quotient between these angles is used to quantify the amount of relaxation of the epilayer. Note that this does not apply to the (004) reciprocal space map since the (004) is parallel to the sample surface. The results are summarized in Table 2.

	(115)	**(004)**	**(335)**
Angle between R.L.P's and normal vector Q_z	0.08˚	0˚	0.31˚
Interplanar angle between (001)	15.79˚	0˚	40.32˚
% Relaxation	**0.5%**	**0%**	**0.8%**

Table 2. Relaxation of epilayer determined from the reciprocal space maps. R.L.P. stands for reciprocal lattice points. Note that the relaxation of the (004) is not determined using this method.

The previous method cannot be applied to (004); the reason for producing its reciprocal space map is to check if the (115) and (335) reciprocal space maps were on the same projection of reciprocal space with the [001] and [110] poles properly lined in the diffraction plane. The distance between the (004) CdTe and (004) InSb peaks is 6.0 μm^{-1} (Figure 22). If the [001] and

[110] poles are properly lined up, then the vertical distance between the (115) and (335) peaks is expected to be five-fourths of the (004) peak distances, i.e. 7.5 μm^{-1}. What is observed for the (115) and (335) peaks are vertical distances of 7.14 μm^{-1} and 7.39 μm^{-1}, respectively. This is within a reasonable range of the expected value.

To determine the epilayer relaxation from an (004) XRD measurement, the peak separation between the epilayer and substrate (004) diffraction peaks is measured from a symmetric ω:2θ scan. The more strained (less relaxed) an epilayer is, the farther the peak separation between the epilayer and substrate peaks. The reason is that as a material is compressed along the in-plane direction, it typically expands in the out-of-plane direction. The amount of expansion is determined by a material's Poisson ratio [45]. Since the epilayer expands in the out-of-plane direction, the diffraction angle of its surface planes, e.g. (004) plane, shifts to lower angles since the interplanar spacing of planes parallel to the surface increases with increasing in-plane strain, as expected from Bragg's law, Equation 4. This is visually depicted in Figure 24 by using RADS to simulate ω:2θ symmetric curves. Peak separation as a function of relaxation is shown in Figure 25.

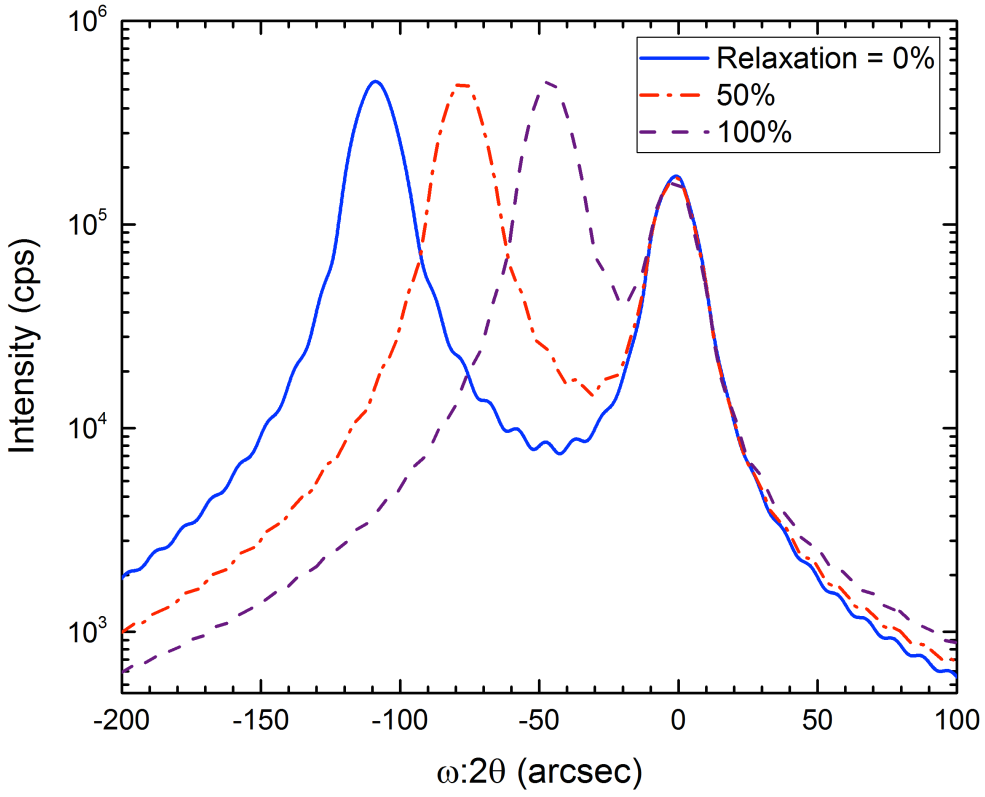

Figure 24. Simulation of (004) symmetric scans for various relaxation values for a 1.8 μm thick CdTe layer on an (001) InSb substrate. RADS is used to generate these curves. Maximum strain corresponds to 0% relaxation and zero strain corresponds to 100% relaxation.

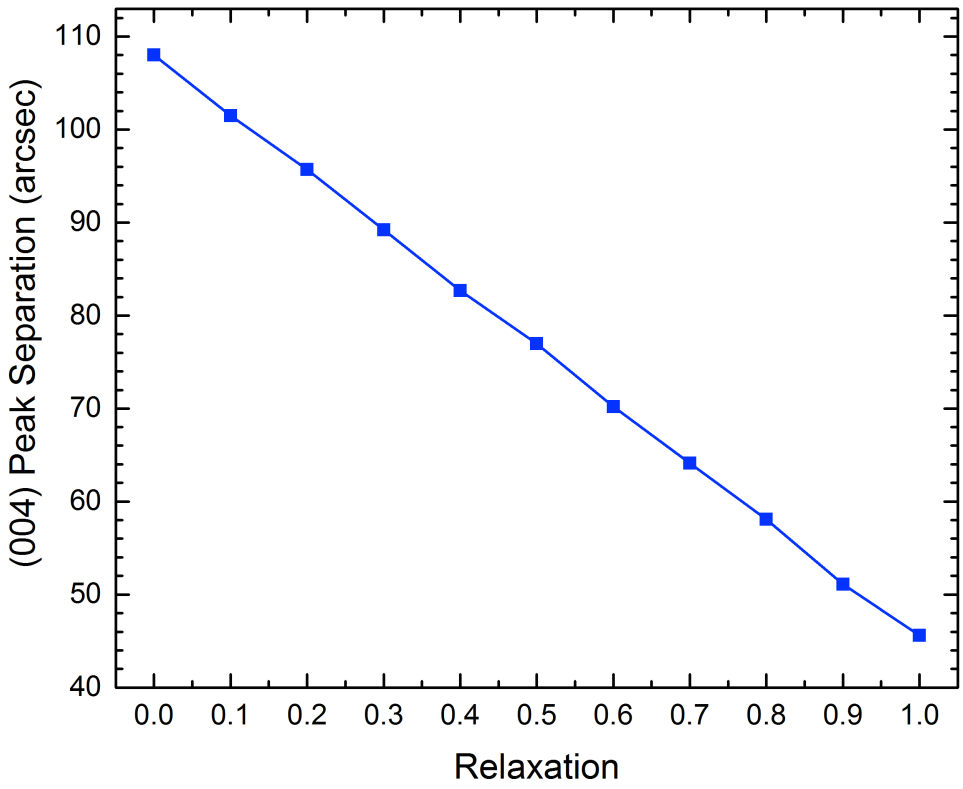

Figure 25. (004) peak separation as a function of relaxation determined by RADS simulations of a 1.8 μm CdTe layer on an (001) InSb substrate. 0% relaxation corresponds to a peak separation of 108.0" and 100% relaxation corresponds to a peak separation of 45.6".

The amount of relaxation can be measured from an (004) scan by correlating the peak separation with the RADS calculations shown in Figure 25. The experimental ω:2θ scan of the (004) peaks is shown in Figure 26.

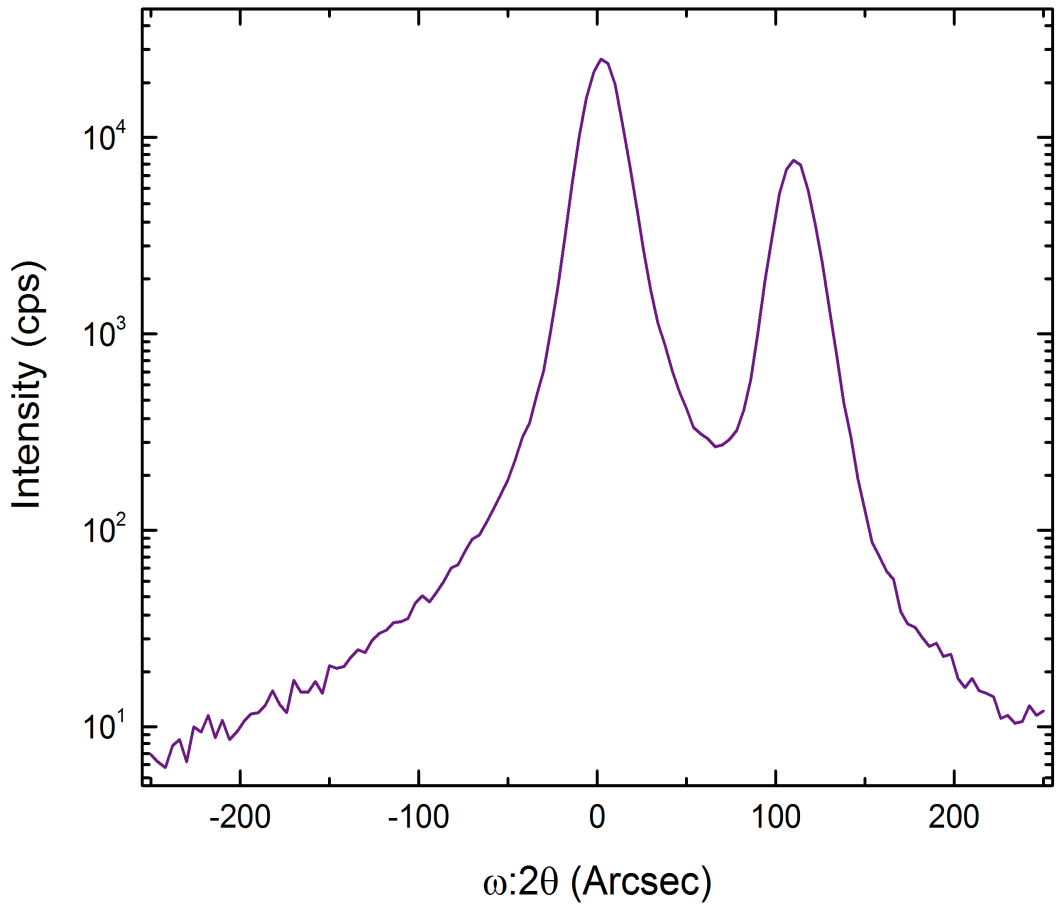

Figure 26. ω:2θ symmetric scan of the (004) peaks. The lattice parameter of CdTe is larger than the lattice parameter of InSb, so the peak on the left is the (004) CdTe peak while the peak on the right is the (004) InSb peak. The peak separation is 108". Scan was done in TAD.

From the (004) symmetric scan, the peak separation is 108", which corresponds to 0% relaxation from Figure 25. The underlying equation used in these simulations is Equation 9. From all measurements of the (115), (004), and (335) peaks, the CdTe epilayer is fully strained by the InSb substrate within a 1% uncertainty. The in-plane lattice parameter of this CdTe epilayer matches the lattice parameter of InSb (6.47937 Å) and the out-of-plane lattice parameter

is 6.486 Å (compared to its intrinsic value of 6.482 Å). The strained out-of-plane lattice parameter was calculated using Equation 9. The Poisson ratio of CdTe is 0.408 [46].

4.3 Afors-Het Simulation Results

The energy band diagram of a CdTe-CdS solar cell is shown in Figure 27. Typical CdTe-CdS solar cells are made up of p-type CdTe and n-type CdS.

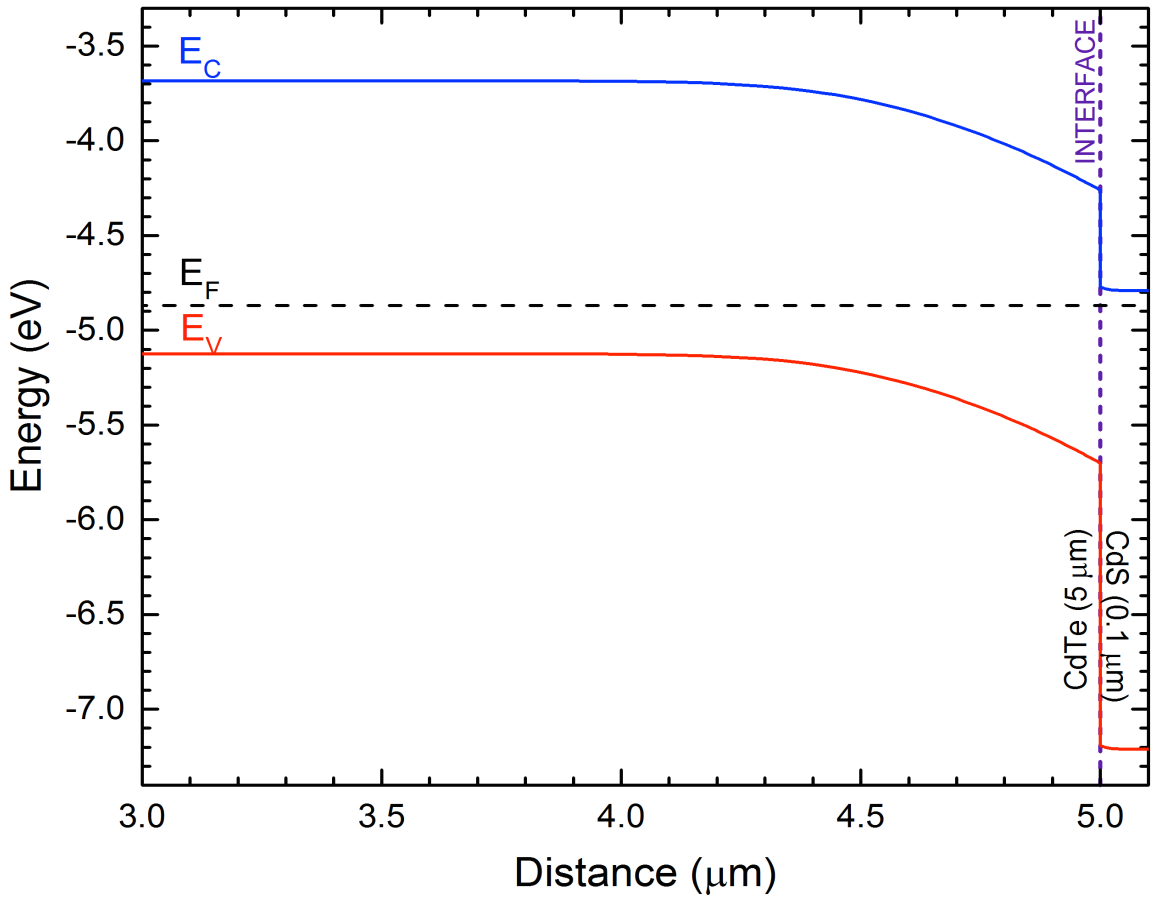

Figure 27. The band diagram of a CdTe-CdS solar. E_C is the conduction band minimum, E_F is the Fermi level, and E_V is the valance band maximum. The total thickness of the CdTe layer is 5 μm, but the first two microns have been truncated in this plot to accentuate the much thinner 0.1 μm CdS layer.

To entertain the local p-n junction hypothesis [7] that suggests grain boundaries can be inverted n-type in a p-type CdTe bulk layer after receiving a $CdCl_2$ treatment, the n-type doping level of two grain boundaries surrounding a p-type grain is simulated. This simulation is applicable to CdTe-CdS devices with grain boundaries parallel to the CdTe-CdS interface, as shown in Figure 17. As the doping of the grain boundaries increases, a trend is observed. At sufficiently high doping levels, a downward slope in energy from the CdTe backside to the CdTe-CdS interface is observed, as shown in Figure 28.

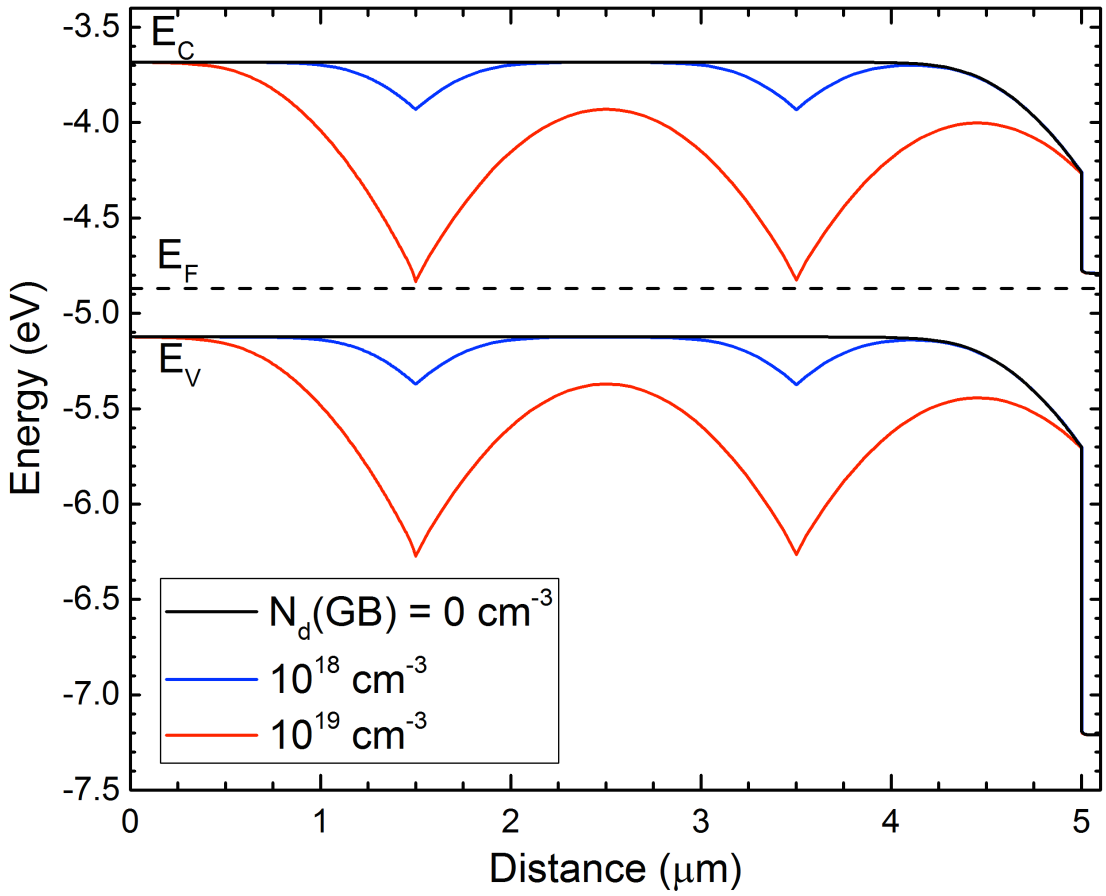

Figure 28. The band diagrams of doping grain boundaries n-type in a p-type bulk CdTe layer generated with Afors-Het. The grain size surrounded by the grain boundaries is 2 μm.

The induced average potential energy and average force of a charged carrier in grain-boundary-doped situation can be calculated. Consider the red curve in Figure 28 that corresponds to a grain boundary doping of 10^{19} cm^{-3}. The energy difference between the CdTe backside (0 μm) and the local maxima near the interface (around 4.5 μm) is the average potential energy within the CdTe layer. The slope between these two points is defined as the average force felt by a conducting charged carrier. A more comprehensive version of Figure 28 is shown in Figure 29.

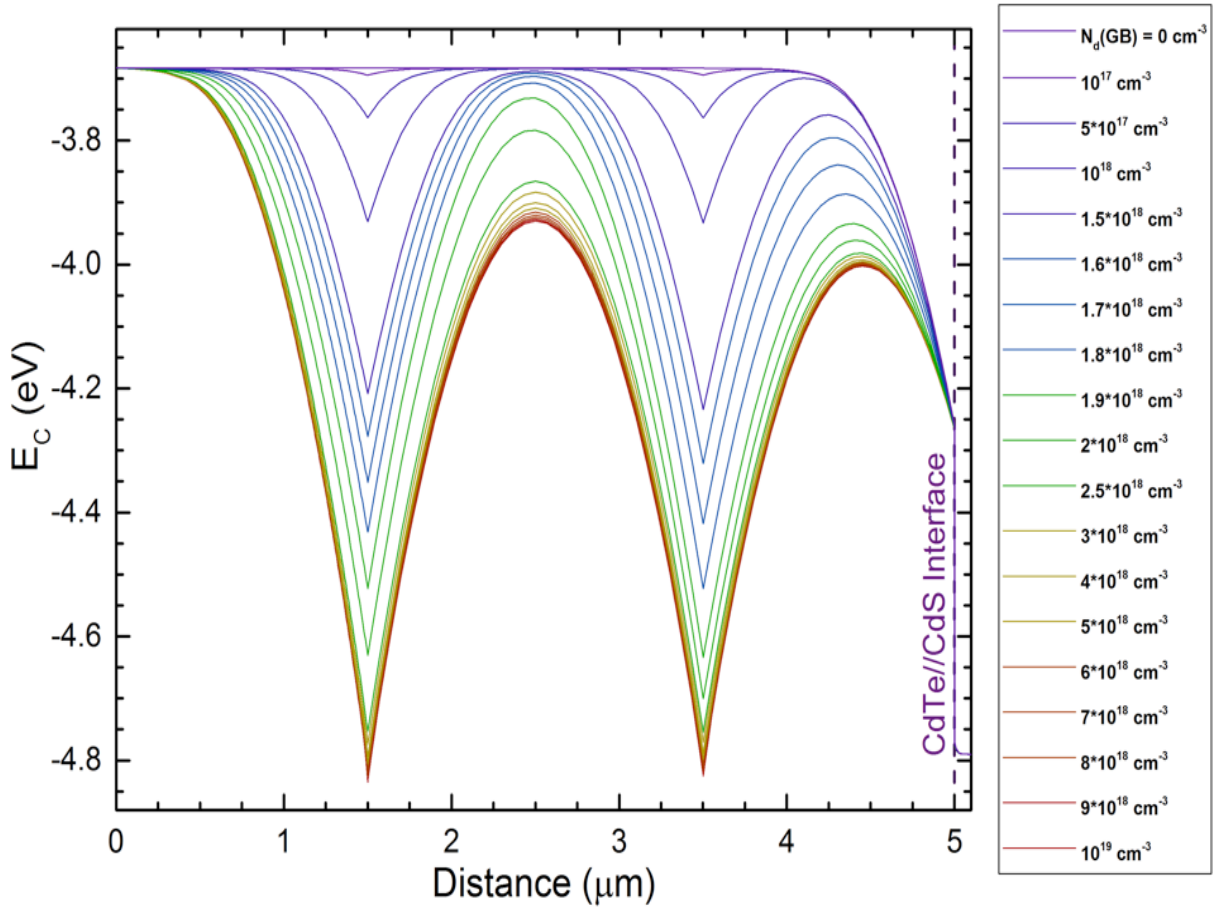

Figure 29. Conduction band profile as a function of grain boundary doping. Since the conduction band and valence band are symmetrical, only the conduction band is shown for clarity. The doping ranges from 0 cm^{-3} to 10^{19} cm^{-3} starting from purple and ending in red, following a rainbow gradient.

From the resulting profiles in Figure 29, the average potential energy and average force on conducting charged carriers is calculated. The results are shown in Figure 30.

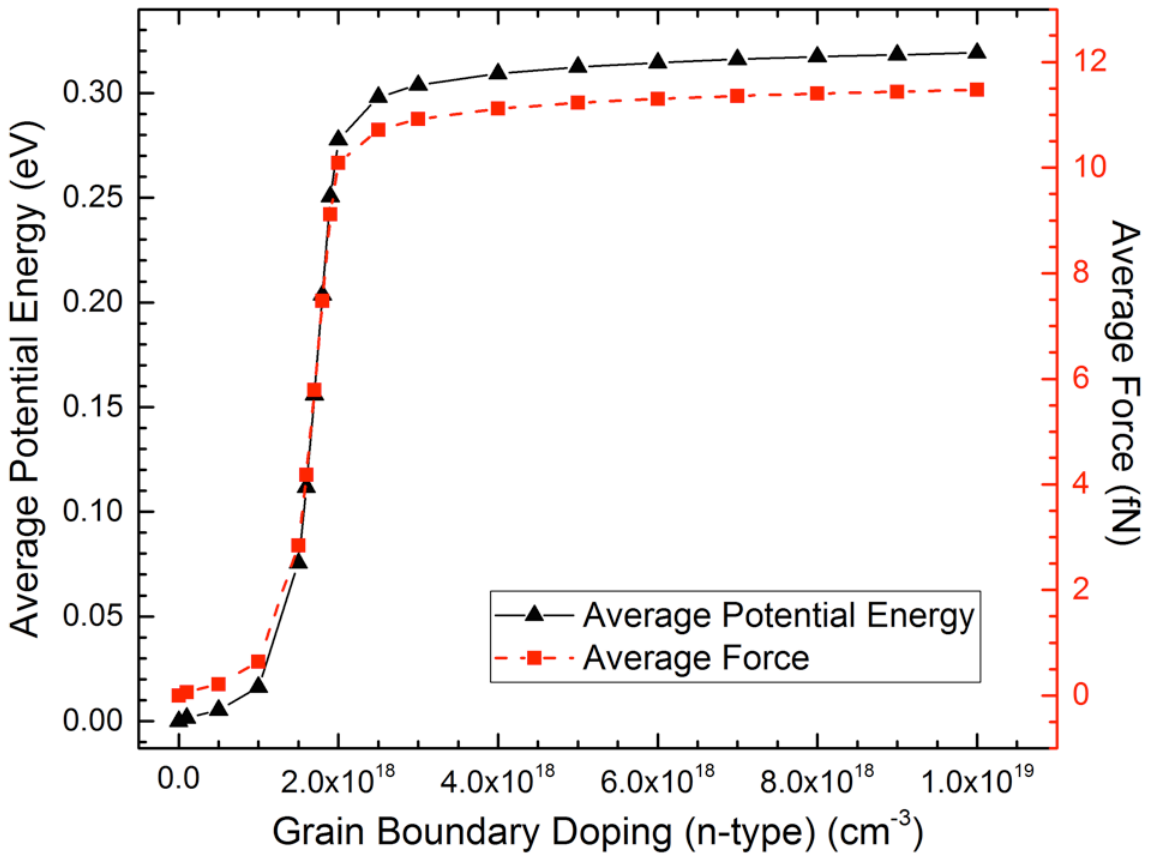

Figure 30. Average potential energy and average force as a function of grain boundary doping.

The increase in potential energy as a function of grain boundary doping appears to follow an exponential relationship. The beneficial effects of local grain boundary doping tapers off at around $2.8 \cdot 10^{18}$ cm^{-3}. These simulations are only applicable for CdTe grain boundaries oriented parallel to the CdTe-CdS interface. One proposed mechanism of how this structure reduces detrimental electron capture at grain boundaries is occupying the harmful interfacial states (see Figure 1) with dopant atoms. The full band diagram of CdTe grain boundaries doped at $2.8 \cdot 10^{18}$ cm^{-3} is shown in Figure 31.

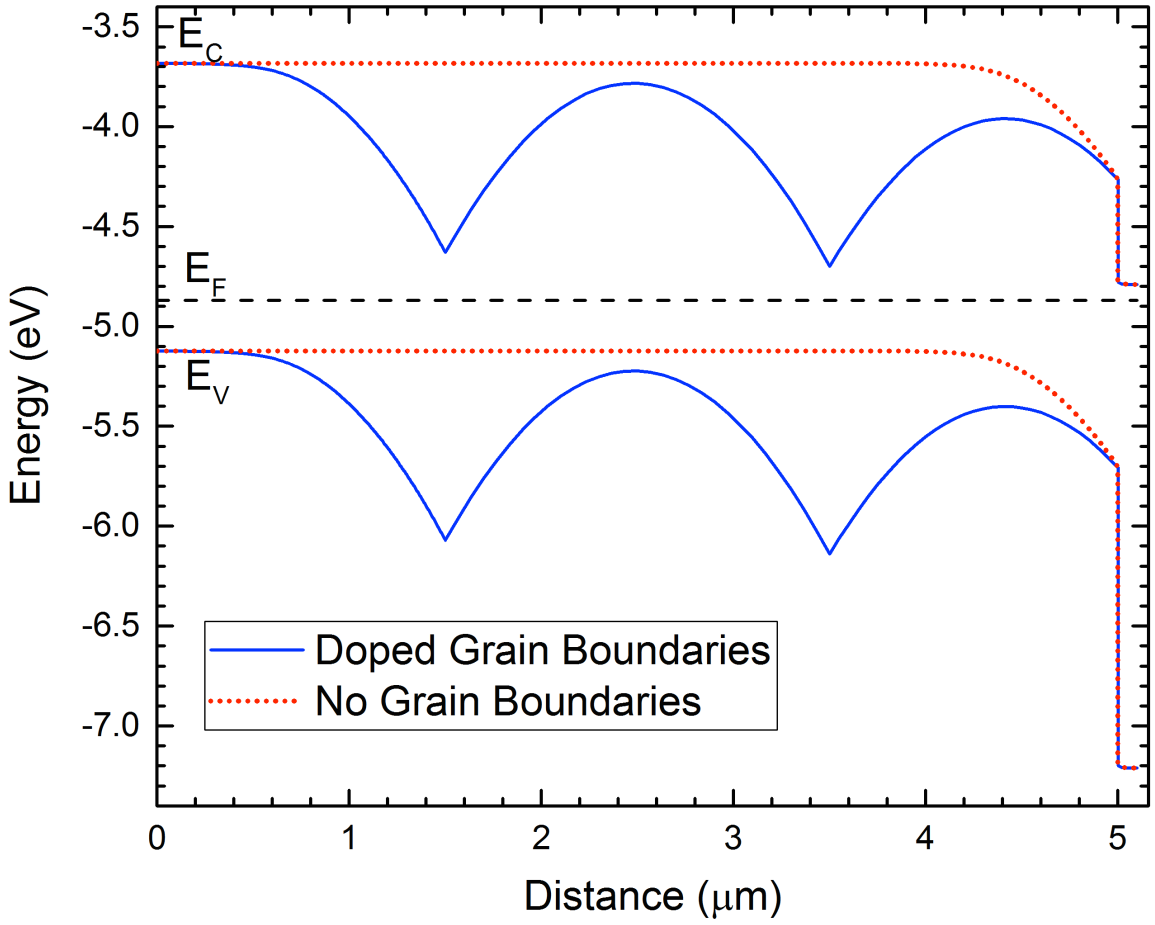

Figure 31. Energy band diagram comparison of CdTe with no grain boundaries and CdTe with n-type doped grain boundaries (doped at $2.8 \cdot 10^{18}$ cm^{-3}) in a CdTe-CdS solar cell.

Chapter 5: Conclusion and Future Work

High quality (001) CdTe epitaxially grown on (001) InSb substrates have been characterized using AFM and HRXRD. The close lattice-match between CdTe and InSb suggests that pseudomorphic structures are possible. The CdTe layer thickness was found to be 1.8 μm and despite the CdTe thickness being slightly larger than the critical thickness, a CdTe on InSb pseudomorphic structure is observed. Relaxation of the CdTe layer was quantified using high-resolution x-ray diffraction methods. For a 0% relaxed (001) CdTe layer on (001) InSb, the in-plane lattice parameter is 6.47937 Å while the out-of-plane lattice parameter is 6.486 Å. These results are crucial for future work in order to make insightful connections between grain boundaries made from wafer bonding and grain boundaries in polycrystalline CdTe.

The exact role of grain boundaries in $CdCl_2$-treated CdTe will be determined through a direct wafer bonding approach. The average RMS roughness of the CdTe surface outside the vicinity of its stacking faults is 0.9 nm, an acceptable roughness fit for wafer bonding. However, wafer bonding cannot be done until the stacking faults are removed first. A precise method for CdTe removal is needed and is in development. A chemical mechanical polishing (CMP) recipe that removes material at rates of less than μm/hr is needed since the CdTe layer is on the order of 1 μm. Furthermore, bringing wafer bonding of CdTe down to room temperature will be attempted as well.

References

1. Y. Y. Loginov, et al., Transmission electron microscopy of CdTe/CdS based solar cells. J. of Crystal Growth 161, 159-163 (1996).
2. First Solar, Inc., "First Solar Press Release 2015 First Solar Achieves World Record 18.6% Thin Film Module Conversion Efficiency," Acquire Media http://investor.firstsolar.com/releasedetail.cfm?ReleaseID=917926 (2015).
3. K. W. Mitchell, et al., Evaluation of the CdS/CdTe Heterojunction Solar Cell. J. Appl. Phys. **48**, 10, 1977.
4. H. Li, et al., Enhanced electrical properties at boundaries including twin boundaries of polycrystalline CdTe thin-film solar cells. Phys. Chem. Chem. Phys. **17**, 11150-11155, (2015).
5. M. G. Spencer, et al., Electrical characterization of grain boundaries in GaAs. Amer. Inst. Phys., **54**, 1429 (1983).
6. W. K. Metzger, et al., Resetting the Defect Chemistry in CdTe. IEEE (2015).
7. C. Li, et al., Grain-Boundary-Enhanced Carrier Collection in CdTe Solar Cells. PRL **112**, 156103 (2014).
8. C. Sun, et al., Creating a Single Boundary between two CdTe (111) wafers with Controlled Orientation by Wafer Bonding. Appl. Phys. Lett. 103, 252104 (2013).
9. J. Lu, et al., Towards defect-free epitaxial CdTe and MgCdTe layers grown on InSb (001) substrates. J. of Crys. Growth 439, 99-103 (2016).
10. V. Bellitto, ed., *Atomic Force Microscopy – Imaging, Measuring and Manipulating Surfaces at the Atomic Scale*. InTech., (2012), "Measurement of the Nanoscale Roughness by Atomic Force Microscopy: Basic Principles and Applications," p. 147.

11. J. R. Taylor, *Classical Mechanics*. University Science Books. (2005), "Oscillations," p. 161.

12. S. Magonov and M. Whangbo, *Surface Analysis with STM and AFM: Experimental and Theoretical Aspects of Image Analysis*. VCH Publishers, Inc., New York (1996), "Scanning Probe Microscopes," p. 31.

13. E. S. Gadelmawla, et al., Roughness Parameters. J. of Mater. Proc. Tech. 123, 133-145 (2002).

14. M. L. Boas, *Mathematical Methods in the Physical Sciences*, 3rd ed. John Wiley & Sons, Inc., (2006), "Fourier Series and Transforms," p. 348.

15. F. Reif, *Fundamentals of Statistical and Thermal Physics*. Waveland Press, Inc., (1965), "Introduction to Statistical Mechanics," p. 24.

16. B. D. Cullity and S. R. Stock, *Elements of X-ray Diffraction*, 3rd ed. Prentice Hall, New Jersey (2001), "Diffraction I: Geometry," p. 90.

17. E. Lifshin, ed. and R. L. Snyder, *X-ray Characterization of Materials*, Wiley-VCH, Germany (1999), "Bragg's Law," p. 25.

18. M. Birkholz, *Thin Film Analysis by X-ray Scattering*, Wiley-VCH, Germany (2006), "High-Resolution X-ray Diffraction," p. 297.

19. O. Madelung, ed., *Semiconductors Other than Group IV Elements and III-V Compounds*, Springer-Verlag, Germany (1992), "Binary Compounds," p. 30.

20. T. Suski and W. Paul, ed., *High Pressure in Semiconductor Physics I: Semiconductors and Semimetals, Volume 54*, Academic Press, California (1998), "Structural Transitions in the Group IV, III-V and II-VI Semiconductors Under Pressure," p. 222.

21. M. E. Straumanis and C. D. Kim, Lattice Parameters, thermal Expansion Coefficients, Phase Width, and Perfection of the Structure of GaSb and InSb. J. of Appl. Phys. 36 (12), 3822 (1965).

22. T. T. Lam, Growth and Process-Related Defects in Mercury Cadmium Telluride Heterostructures [Master's Thesis]. Los Angeles, CA: University of California, Los Angeles; 2001.

23. S. K. Ghandhi, *VLSI Fabrication Principles: Silicon and Gallium Arsenide, 2nd ed.*, John Wiley & Sons, Inc., Canada (1994), "Epitaxy," p. 258.

24. M. Polat, et al., Reciprocal Space Mapping Study of CdTe Epilayer Grown by Molecular Beam Epitaxy on (211)B GaAs Substrate, Mater. Res. Express 4, 035904 (2017).

25. J. M. Oliveira, et al., Nondestructive Monitoring of Defect Evolution in Epitaxial CdTe Thin Layers Grown on Si(111), J. of Phys. Chem., 118, 1968-1973 (2014).

26. S. M. Sze, *Semiconductor Devices: Physics and Tehcnology, 2nd ed.*, John Wiley & Sons, Inc., New York (1985), "Energy Bands and Carrier Concentration in Thermal Equilibrium," p. 17.

27. S. M. Sze, *Semiconductor Devices: Physics and Tehcnology, 2nd ed.*, John Wiley & Sons, Inc., New York (1985), "Carrier Transport Phenomena," p. 47.

28. B. L. Sharma and R. K. Purohit, *Semiconductor Heterojunctions*, Pergamon Press, Oxford (1974), "Theory of Heterojunctions," p. 1.

29. S. M. Sze, *Semiconductor Devices: Physics and Tehcnology, 2nd ed.*, John Wiley & Sons, Inc., New York (1985), "p-n Junction," p. 84.

30. R. E. Hummel, *Electronic Properties of Materials, 3rd ed.*, Springer-Verlag New York, Inc., New York (2001), "Semiconductors," p. 104.

31. Q. Tong and U. Gösele, *Semiconductor Wafer Bonding: Science and Technology*, John Wiley & Sons, Inc., Canada (1999), "Surface Preparation and Room-Temperature Wafer Bonding," p. 49.

32. J. Als-Nielsen and D. McMorrow, *Elements of Modern X-ray Physics, 2nd ed.*, John Wiley & Sons, Ltd., United Kingdom (2011), "Sources," p.29.

33. R. Varache, et al., Investigation of Selective Junctions Using a Newly Developed Tunnel Current Model for Solar Cell Applications, Solar Energy Materials and Solar Cells 131, 14-23 (2015).

34. A. P. Sutton, Models of the Atomic and Electronic Structures of Grain Boundaries in Silicon, Inst. Phys. Conf. 104 (1989).

35. J. Britt and C. Ferekides, Thin-film CdS/CdTe solar cell with 15.8% efficiency. Appl. Phys. Lett. 62, 2851 (1993).

36. M. Gloeckler, et al. Numerical Modeling of CIGS and CdTe Solar Cells: Setting the Baseline. 3rd World Conf. on Photo. Energy Conv. 2003.

37. J. Britt and C. Ferekides,Thin-film CdS/CdTe solar cell with 15.8% efficiency. Appl. Phys. Lett. 62, 2851 (1993).

38. D. W. Palmer, "Properties of the II-VI Compound Semiconductors," D. W. Palmer www.semiconductors.co.uk/propiivi5410.htm (2008).

39. R. K. Swank, Surface Properties of II-VI Compounds. Phys. Rev. 153, 844 (1967).

40. A. M. Goodman, Evaporate Metallic Contacts to Conducting Cadmium Sulfide Single Crystals. J. Appl. Phys. 35, 573 (1964).

41. R. H. Finch, et al., Structure and Origin of Stacking Faults in Epitaxial Silicon, J. of Appl. Phys. 34, 406 (1963).

42. M. L. Boas, *Mathematical Methods in the Physical Sciences*, 3rd ed. John Wiley & Sons, Inc., (2006), "Vector Analysis," p. 276.

43. W. D. Callister, Jr. and D. G. Rethwisch, *Materials Science & Engineering: an Introduction, 9th ed.,* John Wiley & Sons, Inc., (2014), "The Structure of Crystalline Solids," p. 51.

44. D. K. Bowen and B. K. Tanner, *High Resolution X-ray Diffractometry and Topography*, Taylor & Francis, Inc., Bristol, PA (1998), "Triple-axis X-ray Diffractometry," p. 157.

45. W. D. Callister, Jr. and D. G. Rethwisch, *Materials Science & Engineering: an Introduction, 9th ed.,* John Wiley & Sons, Inc., (2014), "Elastic Properties of Materials," p. 177.

46. H. J. McSkimin and D. G. Thomas, Elastic Moduli of Cadmium Telluride, J. of Appl. Phys. 33 (1), 56-59 (1962).